Observed Oceanic Response over the Upper Continental Slope and Outer Shelf during Hurricane Ivan*

W. J. TEAGUE, E. JAROSZ, D. W. WANG, AND D. A. MITCHELL

Naval Research Laboratory, Stennis Space Center, Mississippi

ABSTRACT

Hurricane Ivan passed directly over an array of 14 acoustic Doppler current profilers deployed along the outer continental shelf and upper slope in the northeastern Gulf of Mexico. Currents in excess of 200 cm s^{-1} were generated during this hurricane. Shelf currents followed Ekman dynamics with overlapping surface and bottom layers during Ivan's approach and transitioned to a dominant surface boundary layer as the wind stress peaked. Slope currents at the onset of Ivan were wind driven near the surface, but deeper in the water column they were dominated during and after the passage of Ivan by subinertial waves with a period of 2–5 days that had several characteristics of topographic Rossby waves. Currents on the slope at 50 m and greater depths commonly exceeded 50 cm s^{-1}. Surprisingly, the strongest currents were present to the left of the storm track on the shelf while more energetic currents were to the right of the hurricane path on the slope during the forced stage. Near-inertial motion lasting for a time period of about 10 days was excited by the storm on the shelf and slope. Record wave heights were measured near the eyewall of Hurricane Ivan and were shown not to be rogue waves. The large surface waves and strong near-bottom currents caused significant bottom scour on the outer shelf at water depths as deep as 90 m.

1. Introduction

The Naval Research Laboratory has conducted an intensive measurement program of the outer continental shelf and upper slope waters off the Gulf Coast as part of its Slope to Shelf Energetics and Exchange Dynamics (SEED) project (Mitchell et al. 2005; Wang et al. 2005; Teague et al. 2006a). A major goal of SEED is to understand the physical processes that control the exchange of mass, momentum, heat, and water properties across the shelf break. The shelf gently slopes from the Gulf Coast to the shelf break located at a depth near 100 m, and then depths rapidly drop to greater than 2500 m. With the primary focus on current measurements, six current profiler moorings that also contained wave/tide gauges were deployed in trawl-resistant bottom mounts (TRBMs) on the continental shelf at water depths ranging between 60 and 90 m just west of the DeSoto Canyon, about 100 miles south of Mobile Bay, Alabama. An additional eight deep current profiler moorings were deployed down the slope (Fig. 1). On 16 September 2004 at about 0000 UTC, the center of Hurricane Ivan passed directly over the instrument array (Figs. 1 and 2). Historically, instruments in the ocean often do not survive near misses of such powerful storms, much less direct hits. Fortunately, all of the SEED moorings survived this powerful storm and provided the best ocean measurements of currents and waves ever obtained directly under a major hurricane.

Current and wave measurements directly under hurricanes during their passage have been sparse in the past and lacked sufficient spatial and temporal resolution to investigate the oceanic response in detail (Shay et al. 1989). In addition, due to the difficulty in predicting where hurricanes will appear and where they will travel, most measurements of hurricane-induced currents and waves have been chance encounters by instruments deployed for other purposes. That is the case here as well; however, the location of the array (Figs. 1 and 2) and its configuration with a mean east–west separation of 18 km and a mean north–south separation

Corresponding author address: William J. Teague, Naval Research Laboratory, Stennis Space Center, MS 39529-5004.
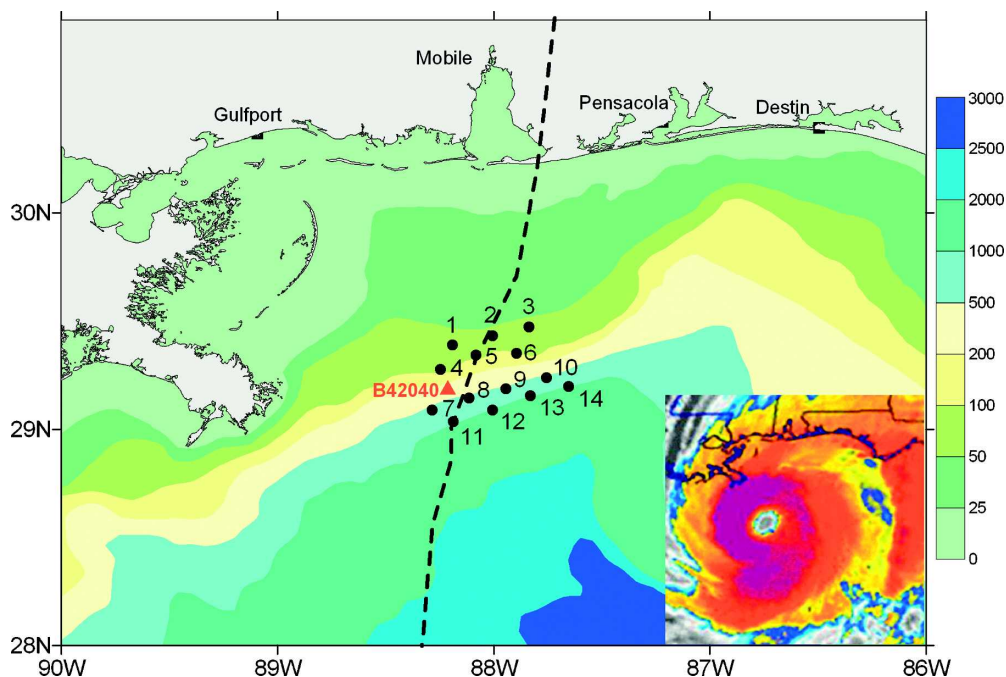E-mail: teague@nrlssc.navy.mil

FIG. 1. Instrument locations (black dots: shelf moorings M1–M6 and slope moorings M7–M14), NDBC buoy 42040 (red triangle), bathymetry (color-filled contours, in meters), and Hurricane Ivan's track (black dashed line) in the northeastern Gulf of Mexico. Inset is a color infrared picture of Ivan taken by the NOAA *Geostationary Operational Environmental Satellite-12* (*GOES-12*) satellite that shows the storm size and the well-defined eyewall.

of 12.5 km was ideal for capturing the directly forced response (Price et al. 1994; Mitchell et al. 2005), surface wave field (Wang et al. 2005), and the "relaxation stage" response following the hurricane.

Knowledge of hurricane-driven currents and waves are very important in the design specifications for offshore structures that may be subject to hurricane conditions (Forristall et al. 1991). Criteria are normally based on extreme conditions that may be expected to occur only once in 100 years. Accurate estimations of extreme conditions are required to realistically model the oceanographic conditions, and hence to develop the correct design standards. According to industry and national weather sources, the damage done by currents and waves during Ivan was on the extreme high end for a category-4 hurricane. Ivan had been the most expensive hurricane ever for the oil and gas industry in the gulf, prior to Hurricane Katrina in 2005. The Minerals Management Service (MMS) reported that Ivan forced evacuation of 75% of the staffed platforms in the gulf (574 platforms) and 59% of the drilling rigs (69 rigs), set adrift 5 rigs, and sunk 7 rigs entirely. The most costly damage was believed to have been made to the underwater pipelines. Aside from obvious leaks, some pipelines were reported to have moved about 915 m while others were buried under 9 m of mud and could not be found. The most extensive damage to the pipelines was attributed to undersea mudslides (equivalent to a snow avalanche) caused by extreme surface waves and hurricane wind-driven currents.

The purpose of this paper is to provide a general documentation of the currents and processes observed in this unique storm dataset and to set the stage for focused studies prompted by these analyses. Thus far, shelf current observations during Ivan have been reported on by Mitchell et al. (2005), the record surface wave was reported on by Wang et al. (2005), and the bottom scour was reported on by Teague et al. (2006b). The air–sea momentum transfer estimated using the hurricane-induced ocean current velocity observations was discussed in terms of the drag coefficient by Jarosz et al. (2007). A description of Hurricane Ivan and scaling parameters that characterize the ocean response are provided in section 2, the instrumentation and hurricane dataset are described in section 3, current statistics are provided in section 4, current observations during the forced stage on the shelf and the slope are described in section 5, the post-hurricane response is discussed in section 6, bottom scour is summarized in section 7, a comprehensive wave discussion is provided in section 8, and a summary and conclusions are given in section 9.
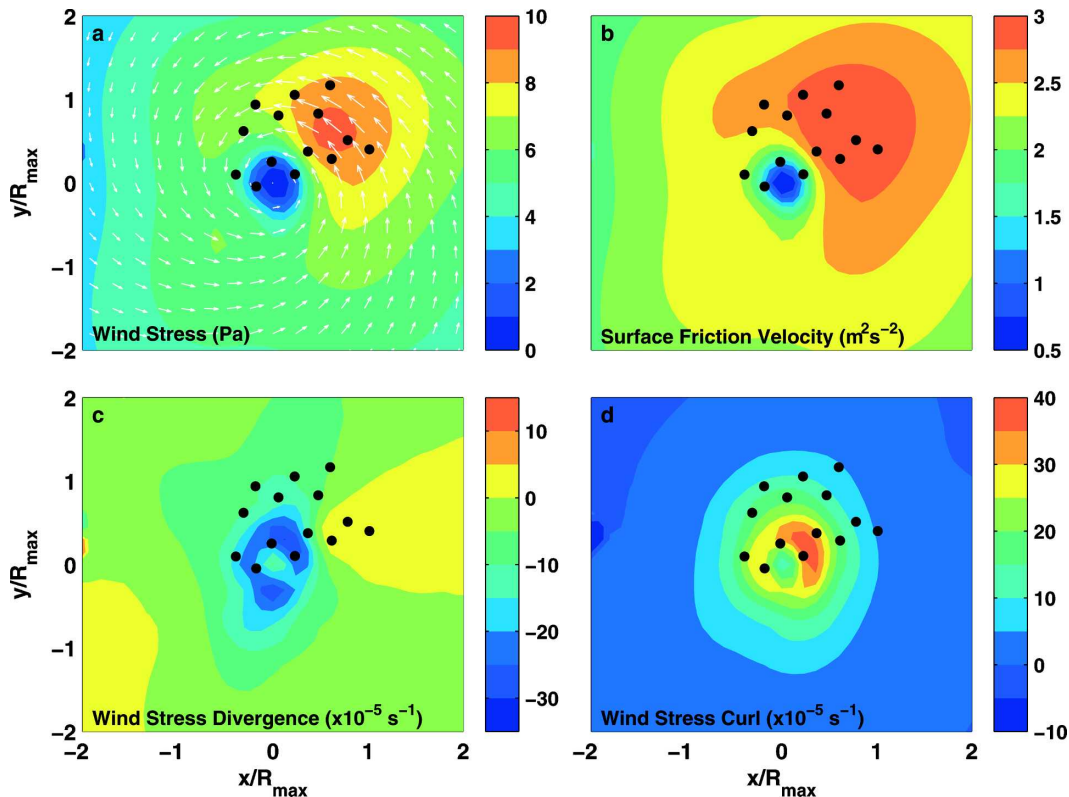
FIG. 2. The eye of Hurricane Ivan, shown here, passed over the moorings at approximately 0000 UTC 16 Sep 2004. (a) Wind stress (Pa) with wind direction arrows, (b) frictional wind velocity ($m^2 s^{-2}$), (c) wind stress divergence (s^{-1}), and (d) wind stress curl (s^{-1}). Mooring locations are indicated by the black dots.

2. Hurricane Ivan

Hurricane Ivan intensified into a category-1 hurricane on 5 September 2004 in the North Atlantic Ocean near 9.7°N, 44.3°W. It entered the Caribbean Sea on 8 September and intensified to category 4. On 14 September, it passed through the Yucatan Strait and entered the Gulf of Mexico on a northwest trajectory and intensified to category 5. On September 16 around 0000 UTC, as a category-4 storm, Ivan veered to the east and passed directly over 14 ADCPs deployed in the Mississippi Bight in support of SEED (Fig. 1) before making landfall near Gulf Shores, Alabama.

The path and speed of the eye changed several times immediately prior to and during its translation over the SEED array. While south of the array its course was slightly northwest with a speed of 6 m s^{-1}, before decelerating to 3.1 m s^{-1} and veering to the north. As the eye passed over the array it accelerated to 4.8 m s^{-1}, veered to the east, and continued to accelerate to 6.8 m s^{-1} before passing out of the array region. Thus, the mean translation speed over the array was about 5.8 m s^{-1}.

Ivan was a category-4 storm with a central pressure in the 932-hPa range and maximum winds of 55–60

m s^{-1} about 40 km from the eye's center, a distance commonly referred to as the radius of maximum winds (R) or the eyewall. Wind stress vectors (Fig. 2a) were constructed from 10-m winds from the NOAA Atlantic Oceanographic and Meteorological Laboratory Hurricane Research Division (Powell et al. 1998) and the Donelan et al. (2004) drag coefficient formulation, in which the drag coefficient peaks at 0.0028 for wind speeds greater than 33 m s^{-1}. The maximum wind stress was about 9.5 Pa at R and 7.5 Pa at 1.5R, respectively, where the estimated friction velocity was between 2.75 and 3 m^2 s^{-2} (Fig. 2b). The wind stress divergence (Fig. 2c) had values of -30×10^{-5} s^{-1} around the eye and more typical values between -5×10^{-5} and 5×10^{-5} s^{-1} elsewhere. The wind stress curl in the cyclonically rotating core of the storm extended out about 2R with a maximum value of 40×10^{-5} s^{-1} near the center, but values greater than 5×10^{-5} s^{-1} only extended out to R (Fig. 2d).

External parameters and scales that can be used to form a qualitative idea of the character of the ocean response (Geisler 1970; Greatbatch 1984; Price et al. 1994) during Hurricane Ivan in the vicinity of the moorings were: hurricane maximum winds of 55–60 m s^{-1},

TABLE 1. Mooring summary: M is the mooring number, geographical position is given by lat and lon (in degrees), the time range of data is between the start and end days, the data sampling interval is dt, the depth of the top velocity bin is $z1$, the depth of the deepest velocity bin is zN, the vertical distance between bins is dz, the depth of water is bottom (all depths in meters), and the instrument utilized is type.

M	Lat	Lon	Start	End	dt	$z1$	zN	dz	Bottom	Type
1	29.39	−88.19	122	305	0.25	6	52	2	60	Workhorse, SBE26
2	29.43	−88.01	122	305	0.25	4	54	2	60	Workhorse, SBE26
3	29.47	−87.84	122	304	0.25	6	54	2	60	Workhorse, SBE26
4	29.28	−88.25	123	304	0.25	10	82	2	88	Workhorse, SBE26
5	29.34	−88.08	123	304	0.25	11	83	2	89	Workhorse, SBE26
6	29.35	−87.89	123	304	0.25	9	81	2	87	Workhorse, SBE26
7	29.09	−88.28	124	311	1.0	52	492	10	511	Long Ranger
8	29.14	−88.11	124	312	1.0	52	492	10	511	Long Ranger
9	29.19	−87.94	124	312	1.0	50	500	10	518	Long Ranger
10	29.24	−87.76	124	312	1.0	51	511	10	530	Long Ranger
11	29.04	−88.19	125	312	1.0	53	493	10	1016	Long Ranger
					1.0	912				AA RCM9
12	29.09	−88.00	125	312	1.0	53	513	10	1038	Long Ranger
					1.0	934				AA RCM9
13	29.16	−87.83	126	312	1.0	50	500	10	1025	Long Ranger
					1.0	921				AA RCM9
14	29.20	−87.65	126	312	1.0	52	502	10	1029	Long Ranger
					1.0	925				AA RCM9

eyewall radius (R) or cross-track scale of 40 km, along-track scale of 81 km, along-track time scale of 8.73×10^4 s^{-1}, translation or forward speed of 5.8 m s^{-1}, maximum wind stress of 9.5 Pa, and Coriolis parameter of 7.2×10^{-5} s^{-1}. In addition, a mixed layer depth (h) of 50 m and a reduced gravity (g') of 0.04 were estimated for this region from historical hydrographic data. Estimates of wind-driven velocity in the mixed layer and isopycnal displacement (Price et al. 1994), which could be generated by Hurricane Ivan, were 1.3 m s^{-1} and 22 m.

Following Price et al. (1994), several nondimensional parameters consisting of the nondimensional storm speed (S), Burger number (B), Mach number (C), and Rossby number (Q) that characterize the response for the open ocean case to a steadily translating hurricane were computed. The ratio of a local inertial period to a hurricane residence time, S, was approximately 1.6 for Hurricane Ivan and, thus, comparable to the local inertial period. As a consequence, the response of the upper ocean should be characterized by strong inertial motions asymmetric across the storm track. The Burger number is a direct measure of a pressure coupling between mixed layer currents and thermocline currents: B was 0.06 for Ivan, implying a rather moderate pressure coupling and a moderately pronounced relaxation stage. The Mach number C is the ratio of storm translation speed to the gravest-mode internal-wave phase speed. Upwelling driven by the wind stress curl, the process responsible for density changes and cooling in the thermocline through divergence of upper ocean,

can by quantified by C, which for Ivan was 2.9 (the gravest-mode internal-wave speed was taken to be 2 m s^{-1}). The estimated Mach number suggested that the upwelling and geostrophic component generated by Hurricane Ivan would be rather modest. The Rossby number Q is given by the ratio of the horizontal advection of momentum to the Coriolis force; Q for the mixed layer currents associated with Hurricane Ivan was about 0.55. This Rossby number is fairly large and indicates that nonlocal or advective effects could be of some importance during the forced and early relaxation stages.

3. Data

Fourteen ADCPs were deployed in May 2004 along the outer continental shelf and slope in the northeastern Gulf of Mexico (Fig. 1). The averaged horizontal spacing between instruments was about 15 km. All of the moorings were recovered in November 2004 and 13 were redeployed at the same locations (M14 was not redeployed because of equipment failure). Final recovery of the moorings was accomplished in May 2005. Table 1 provides positions, times, instrument depths, bottom depths, velocity bin levels, and instrument types.

Six moorings were deployed down the outer shelf in two lines consisting of three moorings, each at depths of 60 m [M1–M3, line 1 (L1)] and 90 m [M4–M6, line 2 (L2)] (Fig. 1). They were deployed in TRBMs, which utilized dome-shaped mounting pods known as Barnies after their barnacle-like shape (Perkins et al. 2000). The

Barny mounts were equipped with RD Instruments Workhorse ADCPs operating at 300 kHz and Sea-Bird Electronics wave/tide gauges. The ADCP heads were situated about 0.5 m off the bottom and recorded current profiles with 2-m vertical resolution every 15 min with an accuracy of $0.5\% \pm 0.5$ cm s^{-1}. The moorings also measured near-bottom pressure and temperature.

Eight moorings were deployed along the continental slope in two lines consisting of four moorings each at depths of 500 m [M7–M10, line 3 (L3)] and 1000 m [M11–M14, line 4 (L4)] (Fig. 1). These moorings consisted of RD Instruments Long Ranger ADCPs operating at 75 kHz contained in 45-inch diameter Flotation Technology buoys. Current profiles of approximately 500 m in vertical extent were measured every hour with 10-m resolution at an accuracy of $1\% \pm 0.5$ cm s^{-1}. The moorings near 500-m depth were deployed 10 m from the bottom and recorded near-full water column current profiles. The moorings near 1000-m depth were located about 500 m above the bottom and hence only measured the upper water column. The eight moorings also measured pressure and temperature at the depth of the ADCPs. Additionally, for the four 1000-m moorings, Aanderaa RCM9 Doppler current meters were located about 100 m above the bottom at about 900-m depth and recorded current speed and direction, temperature, and pressure. Their velocity accuracy is under 1 cm s^{-1}.

The currents and near-bottom temperature data return were excellent and required minimal editing. Removal of measurement error and high-frequency motions, not of interest here, was accomplished by applying a sixth-order low-pass Butterworth filter with a 4-h cutoff frequency. The filter was applied forward and backward to eliminate phase shifts. After low-pass filtering, the amplitude and phase of tidal constituents were computed using the tidal analysis program T_TIDE (Pawlowicz et al. 2002) over the entire half-year deployment period. The principal tidal constituents estimated and removed were K_1, O_1, M_2, N_2, and S_2.

Currents at the shelf break and along the continental slope in the northern Gulf of Mexico often follow the bathymetry (Teague et al. 2006a). The bathymetric contours within the mooring array were approximately parallel and were tilted about 20° counterclockwise from an east to west line (Fig. 1). For most of the analyses performed here, the current data were rotated 20° counterclockwise from east so that u components were along-shelf and v components across-shelf. Positive u values are referred to as upshelf, and negative u values downshelf. Positive and negative v values are referred to as onshelf and offshelf, respectively.

Sea-Bird Electronics Wave and Tide recorders (SBE 26 SEAGAUGE) measured near-bottom pressure (P_b) and wave-induced dynamic pressure (P_w) at the six moorings (M1–M6) on the outer continental shelf. Wave-induced dynamic pressure data (P_w) were collected by burst sampling every 8 h for 512 s with a 1-Hz sample rate. Based on linear wave theory, sea surface wave elevation (η) for a constant water density of 1026 kg m^{-3} was calculated from P_w by applying a frequency-dependent pressure response factor (Dean and Dalrymple 1991) that compensates for exponential depth attenuation effects and projects the near-bottom pressure field to the surface. A cutoff frequency was chosen to avoid contamination due to spurious high-frequency pressure noise amplified by the response factor. An attenuation threshold of 1.5% was empirically chosen for the cutoff frequency so that high-frequency wave components with an attenuation factor less than 1.5% were excluded. The cutoff frequencies were 0.14 and 0.12 Hz for moorings in water depths of 60 and 90 m, respectively. The exclusion of higher-frequency wave components could result in an underestimation of wave energy, but it should be insignificant during high seas when most of the wave energy is in waves with frequencies less than 0.08 Hz. This exclusion could limit the description of the nonlinear characteristics of extreme waves. The pressure response factor derived from nonlinear wave theory may provide more accurate surface wave profiles (DiMarco et al. 2001). Studies to develop and validate a more accurate response factor for the recovery of high frequency waves from attenuated pressure data under extreme seas are needed. However, this is beyond the scope of this work.

4. Current extremes

Hurricane Ivan generated very strong currents on the shelf and slope. Figure 3 shows the current velocity data for 1 day prior to Ivan's arrival and 11 days after Ivan passed through the moorings (between 15 and 27 September 2004). The vertically averaged speeds are shown in Fig. 4. Three-dimensional depictions of the current vectors and winds during the passage of Ivan are shown in Fig. 5. Similar depictions of just the current vectors after the passage of Ivan are shown in Fig. 6. Depth-averaged speeds under Ivan (Fig. 4) increased from east to west on the shelf and from west to east on the slope. On the shelf, strong barotropic velocities (>110 cm s^{-1}) were generated under hurricane winds, while on the slope, somewhat weaker barotropic velocities (<100 cm s^{-1}) were present. There were numerous flow reversals with depth throughout the record in both velocity components (Figs. 3, 5, and 6) over the analyzed time period. After the hurricane passed the cur-
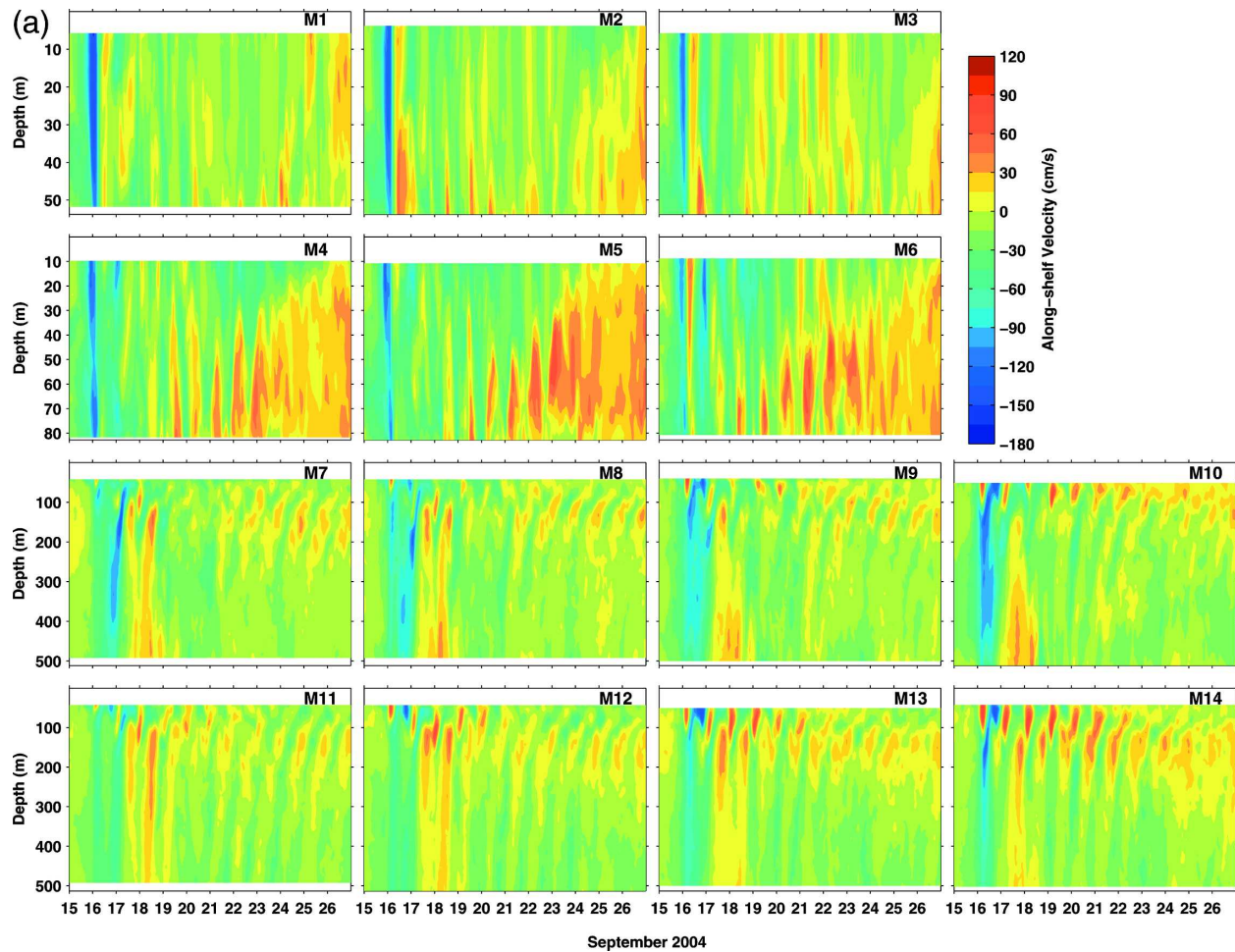
FIG. 3. (a) Along-shelf velocity contours (cm s^{-1}). (b) Cross-shelf velocity contours (cm s^{-1}). Along-shelf and cross-shelf components resulted from a 20° counterclockwise rotation of the east–west and north–south components, respectively. The mooring number is provided on the upper-right side of each panel.

rent records were dominated by near-inertial oscillations modulated by a subinertial frequency motion (Figs. 3 and 6). Both near-inertial and subinertial motions will be discussed in detail in section 6.

Measured current values are useful in model development and in establishing engineering criteria for offshore activities. Current maximums for the raw rotated current data are presented in Table 2 for the time period of 15 to 27 September 2004 (Ivan's eye passed through on 16 September). To conserve table space, statistics for only three to six depth levels are presented but are found to provide a good description of the maximum velocities over depth. Maximum speed (Spd$_{max}$) is computed from u and v and need not correspond to the individual maximum component velocities in Table 2. Maximum direction (Dir$_{max}$, measured clockwise where 0° is north) is the direction that corresponds with the maximum speed.

Current speeds greater than 100 cm s^{-1} were measured at all of the moorings. The maximum speed, 214 cm s^{-1}, at a direction of almost due west (274°) was observed on the shelf in 60 m of water at M1 near the surface (6 m). Similar speeds, ranging between 173 and 196 cm s^{-1}, were found near the surface at the other moorings on the shelf. The maximum speed observed on the slope was 168 cm s^{-1} directed toward 267° at M13 at the top measured depth level of 50 m. Maximum speeds at the other moorings on the slope ranged between 125 and 159 cm s^{-1}. The maximum current speed observed near the bottom on the shelf was 135 cm s^{-1}, occurring at M1 about 8 m off the bottom at a water depth of 60 m. The maximum near-bottom current speed at about the 90-m water depth occurred at M4 and was 131 cm s^{-1} about 6 m off the bottom. All near-bottom maximum speeds on the shelf were at least 98 cm s^{-1}. The maximum near-bottom current speed ob-
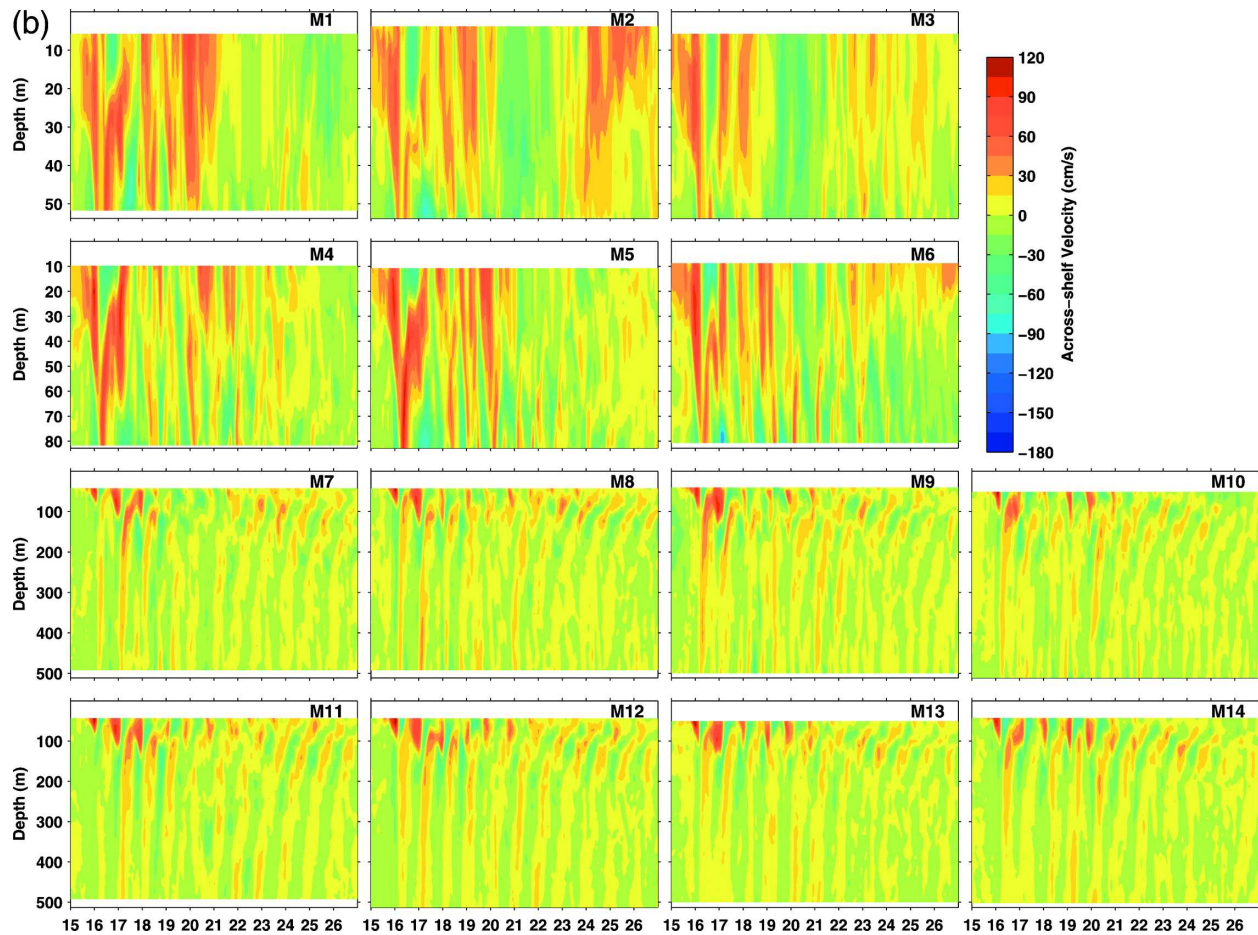
FIG. 3. (*Continued*)

served on the slope was 81 cm s^{-1} at M10. Maximum current speeds generally decreased with depth except for at M8 between 102 and 202 m and at M10 between 51 and 101 m.

5. Forced stage response

Mitchell et al. (2005) in a manner similar to Price et al. (1994) separated the oceanic response to Hurricane Ivan over the outer shelf into four stages based on the magnitude and direction of the wind stress, and then analyzed the first three stages (forced stage response) of the hurricane-forced currents. Stage 1 occurred as Ivan impinged upon the shelf and generated down-welling-favorable conditions (Pedlosky 1987). Stage 2 occurred as Ivan's eyewall crossed the SEED array. Stage 3 occurred as the backside of the storm, behind the eyewall, reached the mooring locations. Stage 4, or "relaxation stage," occurred as the hurricane retreated away from the moorings, and this stage for Hurricane Ivan will be discussed in the next section.

The current response to Hurricane Ivan on the outer shelf has been described by Mitchell et al. (2005). In summary, the current structure on the shelf during stage 1 appeared to be frictionally dominated with overlapping surface and bottom Ekman boundary layers (see Fig. 4 in Mitchell et al. 2005), in agreement with responses to other hurricanes (Keen and Glenn 1994; Shen and Evans 2001). Overlapping Ekman layers suggested that the flow over the outer shelf was not geostrophically balanced during the passage of Ivan. Rapid geostrophic adjustment that is normally associated with the hurricane passage (Price et al. 1994) did not occur on the outer shelf. All six moorings on the shelf recorded onshore advection in the upper water column and offshore advection in the lower water column generated by downwelling (Keen and Glenn 1994). Stage 1 lasted for 15 h and resulted in about a 3°C rise in bottom temperature at each of the shelf moorings (Fig. 7). Then, as the eye of Ivan passed over the moorings in stage 2, the currents made a transition into a dominant surface boundary layer as the wind stress peaked. The
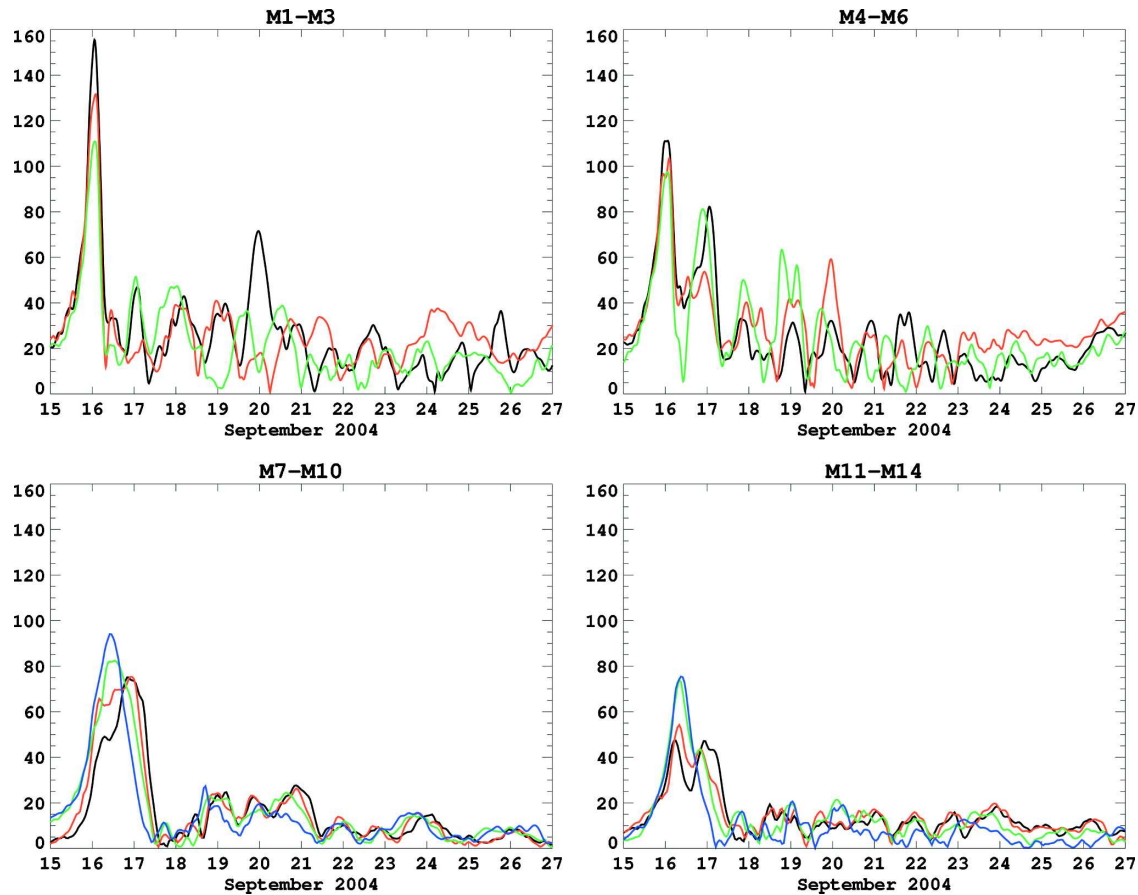
FIG. 4. Depth-averaged speed (cm s^{-1}) vs time in days. Moorings are color-coded from west to east as black, red, green, and blue.

surface Ekman layer rapidly deepened and extended almost to the bottom. Full extension of this layer on L1 (60-m depth) took about 4 h during which the near-bottom velocities veered off-shelf and near-bottom temperatures rose about 4°C. Then the near-bottom currents turned along-shelf aligning with the wind stress, and the flow became nearly barotropic. However, on L2 (90-m depth), bottom Ekman layer currents veered off-shelf and currents at M4 and M5 remained strongly baroclinic. During stage 3, the dominant response was near-bottom onshore flows accompanied by near-bottom temperature decreases. Drops in temperature of about 11°C were observed at M1 and M2 along L1 (Fig. 7a) and at M4 and M5 along L2 (Fig. 7b).

Interestingly, transport per unit width was biased toward the left of the storm track, instead of the right of the track as observed for other hurricanes (Cooper and Thompson 1989; Price et al. 1994), with peak transports of 70, 65, and 53 m^2 s^{-1} and 79, 74, and 70 m^2 s^{-1} from west to east along L1 and L2, respectively. The bias to the left of the track is attributed to the coastal geometry, and in particular to the "boot" shape of the tip of

Louisiana, in which the shelf changes from a broad shallow shelf to a narrow steep shelf over a short distance. Hence, outflows forced by the hurricane winds were squeezed by the boot. This type of effect has also been discussed by Forristall (1980), Keen and Allen (2000), and Keen and Glenn (1995, 1999).

On the slope, during stage 1 (Figs. 5a–c), there was a nearly linear rise in near-bottom temperature about 0.5°C at 500 m (Fig. 7c) and about 0.25°C at 900 m (Fig. 7e), suggesting a presence of downwelling as it was observed on the outer shelf (Mitchell et al. 2005). The structure of the currents, however, did not display well-defined onshore flow in the upper part of the water column and offshore flow below, especially at the beginning of stage 1 (Fig. 5a). During this part of stage 1, both current components were rather weak and showed a lot of variability in flow direction with increasing water depth. With passing time, the wind stress increased from about 1.8 to 5.5 Pa over the slope moorings. Near the end of stage 1 (Fig. 5c), the downshelf flow strengthened and it was well established at and below 100 m at all slope locations. The downshelf-flowing
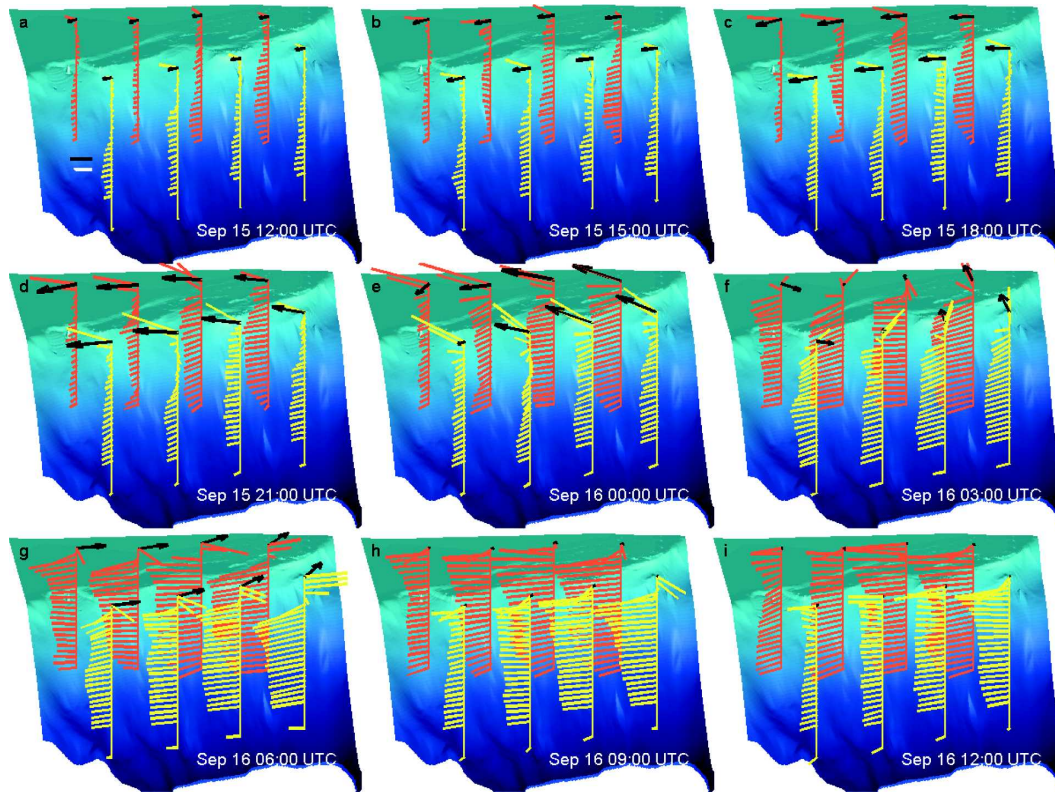
FIG. 5. Current and wind stress vectors for moorings M7–M14 on the continental slope every 3 h beginning at 1200 UTC 15 Sep. Red vectors denote the 500-m line and yellow vectors denote the 1000-m line. The black vectors represent the wind stress. The white and black lines on the lower-left side of (a) represent a current velocity of 50 cm s^{-1} and a wind stress of 4 Pa. (a)–(c) Ivan impinged on the slope moorings in stage 1. (d)–(f) Ivan's eyewall passed over the moorings in stage 2. (g)–(i) The backside of Ivan passes over the moorings in stage 3.

slope currents were stronger at the moorings located on the right side of Ivan's track and tended to increase with depth. At the same time, strengthening of the flow up to 50 cm s^{-1} and an indication of a deepening of the Ekman surface layer began to be visible in the upper part of the water column.

During stage 2 (Figs. 5d–f), the wind stress reached its peak of about 9.5 Pa around 0000 UTC 16 September (Fig. 5e) and started rotating counterclockwise at moorings M7, M8, and M11, while clockwise rotation was observed at the other slope locations. Largest currents were measured during stage 2 at the top of the current profiles. The near-bottom temperatures also reached their maximums at 500 and 900 m with the largest increase at M10 (about 2°C) along L3 (Fig. 7c) and at M14 (about 0.5°C) along L4 (Fig. 7e). The deepening of the Ekman surface layer continued and the clockwise rotation of the currents with depth became more apparent and better resolved. The thickness of this layer varied and decreased westward. Along L4, the maximum thickness was at M14 (about 120 m) and the minimum thickness was at M11 (about 70 m), and

similarly along L3, maximum and minimum thicknesses of about 90 and 60 m were observed at M10 and M7, respectively. The Ekman surface layer currents, whose speeds reached over 100 cm s^{-1} at 60 m and above during stage 2, also began to rotate inertially. Below the Ekman surface layer there was well-established downshelf flow whose velocities increased eastward where they peaked at about 100 cm s^{-1} at M10 and about 80 cm s^{-1} at M14. At the end of stage 2 (Fig. 5f), the currents just below the Ekman surface layer also showed very distinct maxima. Depths of these strong currents varied from one mooring to another but their depth increased eastward; for example, at M11 they were between 70 and 140 m, while at M14 they were between 150 and 220 m. Currents measured near 900 m decreased in magnitude by about 50% from those at 500 m.

The deep current maxima were still present during stage 3 (Figs. 5g–i). The hurricane winds died down significantly over the mooring array with the wind stress dropping down below 1 Pa during this stage. There was also an indication that the Ekman surface
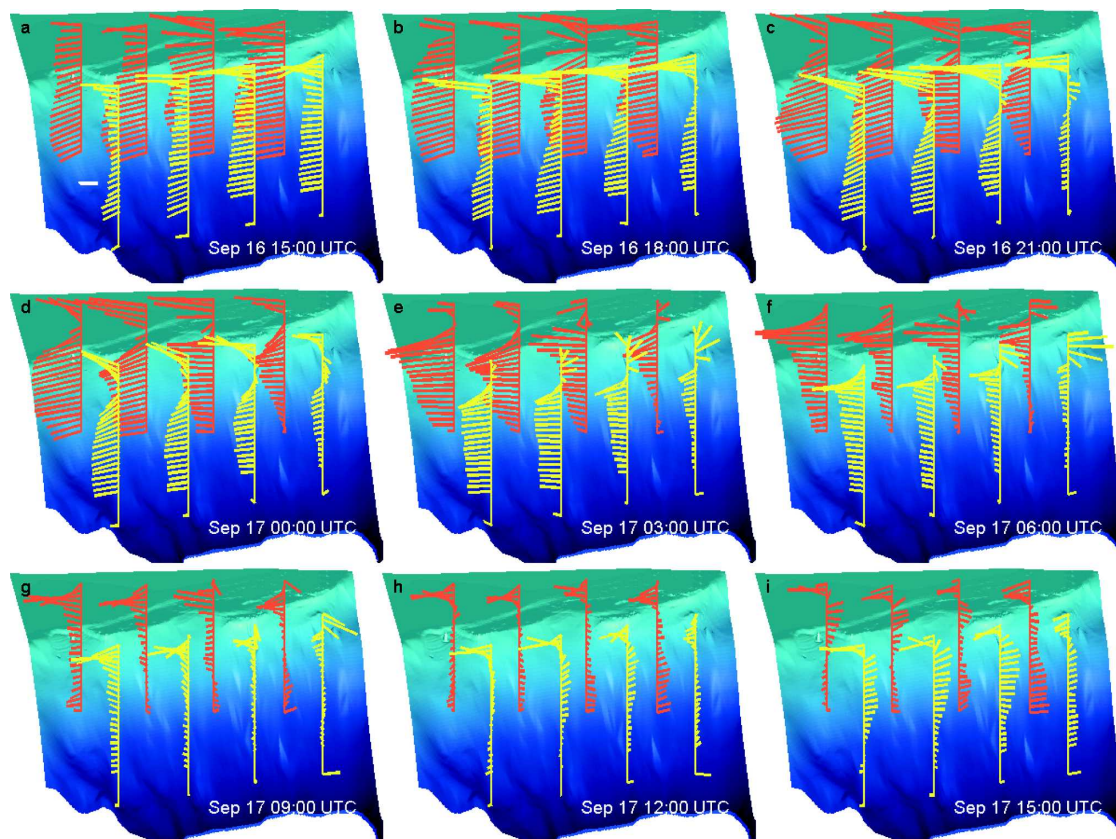
Fig. 6. Current vectors for moorings M7–M14 on the continental slope every 3 h beginning at 1500 UTC 16 Sep in the relaxation stage. Red vectors denote the 500-m line and yellow vectors denote the 1000-m line. The white line on the lower-left side of (a) represents a current velocity of 50 cm s^{-1}. In the relaxation stage, Ivan has retreated from the moorings and subinertial waves, with characteristics of TRWs, become evident in addition to near-inertial motion.

layer began to decrease in thickness at all slope locations. The clockwise rotation with time was still present in the upper part of the water column while below 150 m the downshelf flow with a weaker, mostly onshelf component was still well established. This deep onshelf flow probably attributed to an observed near-bottom temperature decrease (Fig. 7). The largest temperature drop was recorded at moorings M14 (about 0.25°C) (Fig. 7e) and M10 (about 1.5°C) (Fig. 7c). Near the end of stage 3, however, the temperature began to increase again at all locations.

Unlike on the outer shelf, the forced response along the continental slope was biased toward the right of the storm track during these three stages. The strongest currents, largest temperature rise and drop, and thicker Ekman surface layers were recorded at the locations east of the hurricane path, with peak transports per unit width of 338, 339, 379, and 433 m^2 s^{-1} at moorings M7, M8, M9, and M10, and 213, 255, 332, and 347 m^2 s^{-1} in the upper 500 m at moorings M11, M12, M13, and M14. The rightward-biased response has been commonly ob-

served during other hurricanes (see, e.g., Sanford et al. 1987; Church et al. 1989; Price et al. 1994) and arose because the hurricane wind rotates clockwise on the right side of the storm track.

Moving hurricanes have been found responsible for cooling of the sea surface (Emanuel 1988). This forced cooling of the sea surface was observed after passage of Hurricane Ivan (Stone et al. 2005) and, similar to the ocean current response, it showed a strong asymmetry with a rightward bias. Hydrographic data collected during other storms, as well as hurricane models, have showed that there is also appreciable rightward-bias cooling below the sea surface, in the mixed layer, and below in the thermocline due to vertical mixing and advection (Price et al. 1994). Associated with this cooling, enhanced currents in the thermocline have also been observed (Shay et al. 1989; Price et al. 1994). Unfortunately, our data do not include hydrographic measurements for the entire water column to evaluate the cooling below the sea surface for Hurricane Ivan. There was, however, indirect evidence in the current data,
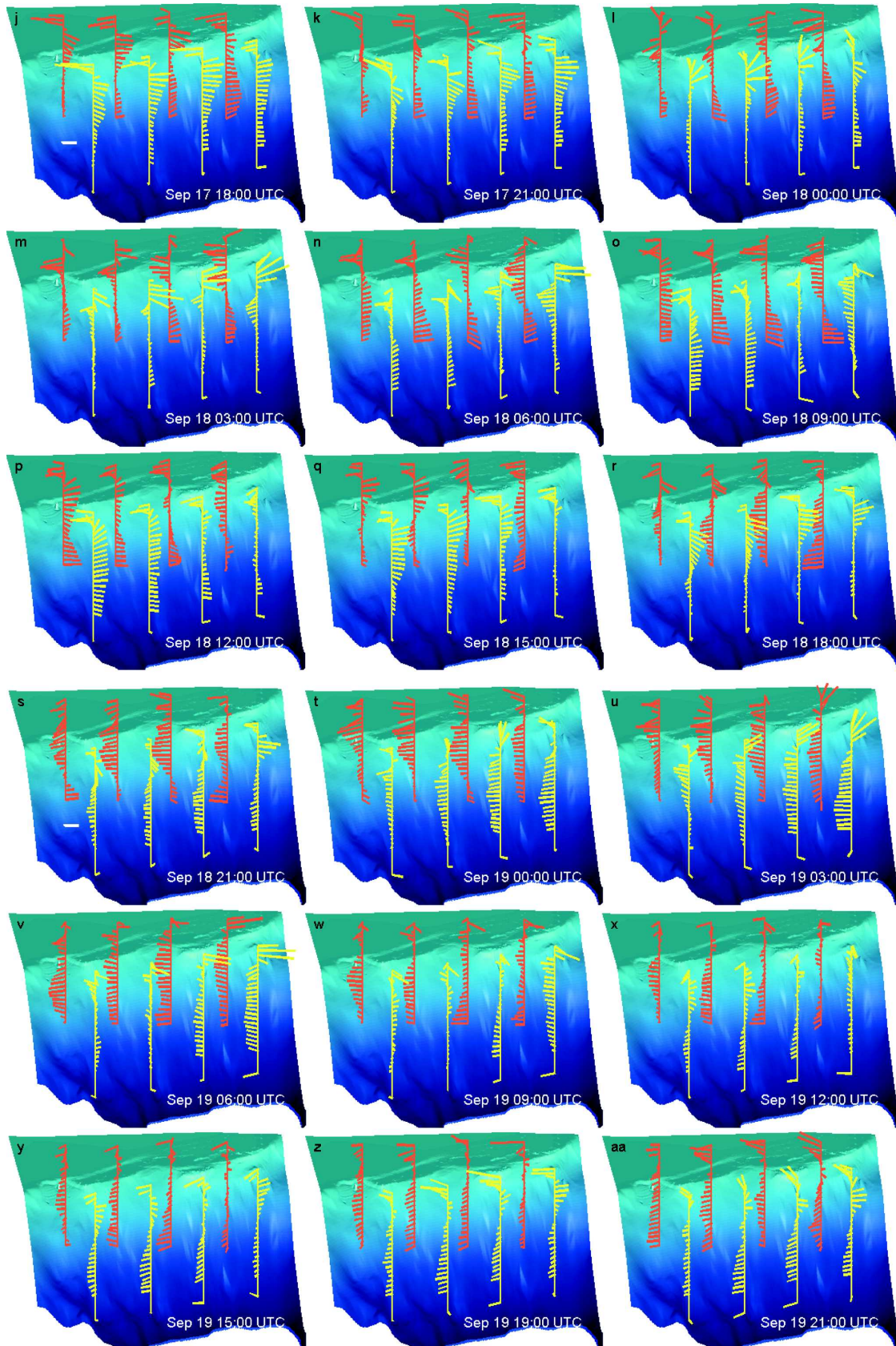
FIG. 6. (*Continued*)

TABLE 2. Statistics for minimum and maximum currents observed. The mooring number is provided in the left column, Z is the observation depth (in meters), and U_{min}, U_{max}, V_{min}, and V_{max} are the minimum and maximum east–west and north–south velocities (in centimeters per second) observed, respectively; Spd_{max} is the maximum speed observed and Dir_{max} is the corresponding direction (in degrees).

	Z	U_{min}	U_{max}	V_{min}	V_{max}	Spd_{max}	Dir_{max}
M1	6	−198.49	64.42	−84.55	98.91	213.95	274.13
M1	30	−152.91	34.14	−40.95	84.25	171.47	277.24
M1	52	−125.69	53.15	−59.47	89.94	134.89	272.12
M2	4	−156.08	45.48	−84.56	116.96	186.84	286.77
M2	30	−135.35	39.12	−43.43	79.26	145.23	275.33
M2	54	−114.75	60.38	−74.40	69.58	120.49	267.76
M3	6	−155.20	50.78	−71.28	123.32	173.02	276.24
M3	30	−112.72	30.64	−52.35	96.97	140.12	286.71
M3	52	−85.61	61.57	−41.45	70.03	98.34	279.48
M4	10	−167.98	32.06	−77.83	155.53	195.56	302.68
M4	30	−130.86	39.82	−43.35	136.94	176.85	300.74
M4	50	−105.19	43.98	−47.71	84.58	125.89	283.32
M4	82	−119.55	54.67	−59.80	77.46	130.90	225.96
M5	11	−152.11	53.34	−76.94	176.59	190.72	317.81
M5	31	−125.60	46.10	−37.56	116.47	158.45	296.42
M5	51	−98.64	76.37	−34.49	111.75	123.04	315.26
M5	83	−110.30	62.37	−72.62	106.58	112.04	238.76
M6	9	−116.48	67.17	−97.38	150.87	181.75	283.13
M6	31	−112.03	55.42	−37.41	134.30	158.37	308.00
M6	51	−83.64	78.23	−49.89	89.42	120.51	297.90
M6	81	−79.68	44.42	−97.16	65.30	102.72	178.94
M7	52	−85.88	16.77	−42.77	117.22	127.16	317.20
M7	102	−125.23	46.66	−35.52	58.68	125.38	252.84
M7	202	−120.74	35.22	−35.76	37.50	122.79	260.48
M7	302	−101.59	26.86	−20.47	30.82	102.58	242.04
M7	492	−65.88	31.24	25.95	26.08	67.68	236.76
M8	52	−107.74	44.08	−61.87	107.09	135.07	287.09
M8	102	−102.01	48.62	−42.85	67.06	103.79	239.36
M8	202	−124.25	28.81	−44.91	26.70	132.12	230.13
M8	302	−83.96	22.18	−24.77	28.75	84.77	242.07
M8	492	−79.26	42.92	−25.10	30.45	79.26	250.47
M9	50	−133.80	80.68	−59.02	100.89	159.14	282.78
M9	100	−110.86	39.00	−44.47	100.74	120.10	307.01
M9	200	−106.84	18.12	−21.33	38.46	107.11	254.07
M9	300	−89.14	10.46	−22.64	30.87	89.53	255.31
M9	500	−69.64	30.92	−53.37	24.68	69.71	252.55
M10	51	−133.53	78.34	−59.05	119.76	134.80	257.88
M10	101	−137.09	75.09	−28.05	77.14	141.86	264.90
M10	201	−112.59	12.45	−27.73	31.00	113.90	258.71
M10	301	−106.16	19.83	−17.96	25.19	108.72	263.40
M10	511	−81.08	44.66	−36.83	27.02	81.90	250.85
M11	53	−90.99	28.06	−52.14	114.64	124.92	300.44
M11	103	−103.69	51.96	−42.94	79.63	103.89	246.40
M11	203	−56.92	40.69	−39.97	28.91	61.52	227.70
M11	303	−56.99	33.91	−27.20	24.05	57.22	255.11
M11	493	−48.01	18.27	−15.75	22.09	48.01	250.66
M11	912	−38.57	18.64	−19.23	20.74	39.33	261.29
M12	53	−125.72	54.90	−68.60	118.55	150.57	283.99
M12	103	−82.13	77.49	−65.52	67.40	91.66	28.83
M12	203	−55.35	28.95	−29.00	32.28	59.44	278.42
M12	303	−58.25	23.86	−18.78	24.50	60.40	265.35
M12	513	−49.41	19.34	−14.19	19.85	50.73	236.91
M12	934	−38.33	18.47	−16.53	19.21	38.71	258.10

TABLE 2. (Continued)

	Z	U_{min}	U_{max}	V_{min}	V_{max}	Spd_{max}	Dir_{max}
M13	50	−160.01	58.41	−60.99	125.84	167.59	267.30
M13	100	−102.01	72.44	−47.80	92.48	121.36	297.96
M13	200	−83.13	36.53	−26.22	25.31	84.95	261.88
M13	300	−71.21	20.27	−16.73	22.84	72.17	261.07
M13	500	−58.29	19.49	−17.16	18.93	58.33	256.42
M13	921	−40.15	22.12	−22.91	19.16	41.28	236.54
M14	52	−154.61	63.58	−70.91	94.16	154.62	250.66
M14	102	−112.70	93.68	−47.37	71.96	115.93	265.70
M14	202	−97.60	35.49	−30.07	40.12	97.60	249.80
M14	302	−86.07	19.61	−18.74	20.73	86.61	256.45
M14	502	−63.95	19.53	−14.89	21.48	64.17	254.73
M14	925	−39.00	29.87	−25.07	22.90	39.03	252.10

where substantial currents at depths between 70 and 220 m were present and were suggestive that such cooling occurred in the thermocline. Based on historical hydrographic data, the thermocline in this part of the Gulf of Mexico is usually observed at depths between 60 and 150 m. Thus, during Hurricane Ivan, the recorded energetic currents between 70 and 220 m were probably located in the thermocline as a response to cooling associated with upwelling there. They first occurred under the back side of Hurricane Ivan (Figs. 5g–i) and indicated the arrival of Stage 4 or a relaxation stage response of the ocean to this hurricane.

6. Post-hurricane relaxation stage

The relaxation stage usually begins after the hurricane passes and can last for several days or weeks (Price et al. 1994). It is impossible to precisely establish when this stage ended for Hurricane Ivan since several other storms (Hurricane Jeanne, Tropical Depression Ivan) impacted the SEED moorings shortly after Hurricane Ivan. Therefore, for this reason, only the data collected between 13 and 27 September 2004 were analyzed for this section, unless stated otherwise.

a. Near-inertial motion

The most distinctive feature of the relaxation stage is usually a three-dimensional wake of near-inertial internal waves. These waves have been recorded in the wakes of several hurricanes (Brooks 1983; Shay and Elsberry 1987; Brink 1989). The nondimensional storm speed of Hurricane Ivan was 1.6, comparable to the local inertial period. Thus Ivan's wake should include strong, asymmetric across-storm-track inertial motions. As confirmed by the SEED time series of u and v (Fig. 3), the passage of Hurricane Ivan generated strong near-inertial motion.

Spectral analyses of the current components (not shown) implied that a major part of the near-inertial
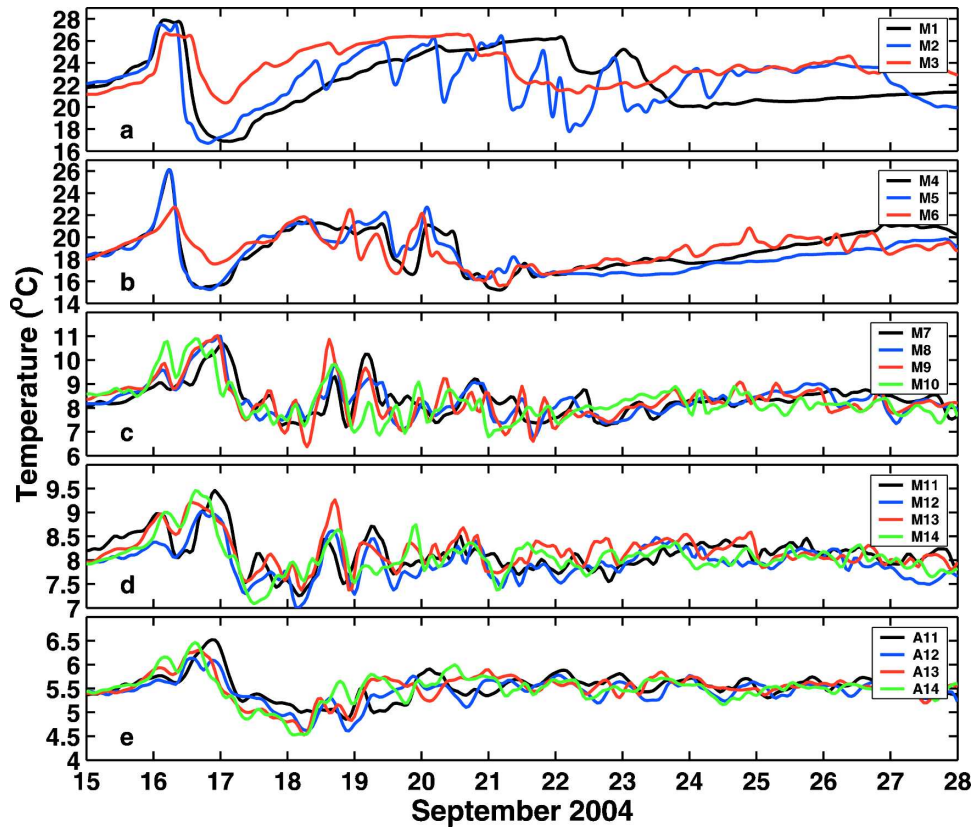
FIG. 7. Near-bottom temperatures for moorings at (a) 60, (b) 90, and (c) 500 m and temperatures at approximately (d) 500 and (e) 900 m for moorings at 1000 m.

energy was contained in the clockwise (CW) rotating component. On the outer shelf, the CW energy estimates at the near-inertial frequency were at least twice as large as estimates of the counterclockwise (CCW) energy, while on the slope, the CW rotating motion was at least one order of magnitude larger than the CCW rotating currents if the spectral peak at the near-inertial frequency for a given depth was above the background noise, that is, statistically significant. Additionally, the spectral analysis suggested that the near-inertial frequency was generally above the local Coriolis parameter (f).

Near-inertial motion is defined to have a frequency between $0.9f$ and $1.2f$ (Kunze 1985). Price (1983) has demonstrated that the frequency of the near-inertial oscillations in the mixed layer is above the local inertial frequency by an amount approximately equal to one-half of the mixed layer Burger number (MLB) given by

$$\text{MLB} = (1 + \tilde{S}2)g'h(2R\tilde{f})2, \qquad (1)$$

where all variables in (1) are defined in section 2. The MLB for Hurricane Ivan was roughly 0.08 and implied that there should be a 0.04 shift in the inertial

frequency above the local Coriolis parameter. It has been also demonstrated (Mooers 1975; Kunze 1985) that the effective frequency of the near-inertial motion (f_{eff}) can be shifted above the local Coriolis parameter (f) by the relative vorticity (ζ) of the mean flow ($f_{\text{eff}} = f + \zeta/2$). The SEED mooring spacing did not allow an estimation of the vorticity for each mooring. However, the vorticity was evaluated separately for the outer shelf and slope for the mean flow observed between 7 and 27 September 2004. On the outer shelf, the vorticity was near 0 above 35 m and positive below, while along the slope, the vorticity was positive above 350 m, where the near-inertial motion was strong, and near 0 or negative below 350 m, where the near-inertial motion was rather weak. Thus depth-averaged vorticities of 1.97×10^{-6} and $8.97 \times 10^{-7} \text{ s}^{-1}$ for the outer shelf and slope, respectively, were used to estimate the effective frequency of the near-inertial motion for the SEED moorings. The effective near-inertial frequency evaluated from direct measurements of ζ was roughly 4% and 9% above the Coriolis parameter at the slope and outer shelf locations, respectively, and was approximately in agreement with the shift in the inertial frequency sug-

gested by the MLB, which did not require current measurements to be evaluated.

To isolate the near-inertial component generated by Hurricane Ivan in the current data, the current velocity components were demodulated at the f_{eff} (Emery and Thomson 2001). Amplitudes of the CW rotating velocity component are displayed in Fig. 8. Amplitudes of the CCW component (not shown) were generally weaker than those of the CW component, and on the slope, the maximum CCW amplitudes were less than 10 cm s^{-1}, while on the outer shelf, they were below 13 cm s^{-1}. Near-inertial oscillations were present prior to the arrival of Hurricane Ivan on the shelf (L1 and L2) (Fig. 8) but were rather weak with amplitudes of 5 to 10 cm s^{-1}. They were absent in the deep water down the slope several days prior to Ivan (L3 and L4) (Fig. 8) but were quite prominent with its passage. An increase in the CW amplitude following the hurricane passage was observed generally at all locations. There was also clear asymmetry about the storm track; that is, the more energetic near-inertial motions were present on the right side of the track. Additionally, the CW motions were stronger and lasted longer on the slope than those observed on the outer shelf. The maximum amplitudes on the slope reached speeds as high as 50 cm s^{-1} at depths above 100 m and had a secondary maximum up to 25 cm s^{-1} at approximately 150 m. There was also a clear indication that vertical structure of the CW amplitude changed with time. Along the slope, the maximum CW amplitudes decreased in strength after about 2 to 4 days or 2 to 4 inertial periods in the upper water column (between 50 and 200 m). After reaching a minimum around 21 September, they began to increase again and another burst of the near-inertial motion occurred around 23 September and lasted until 27 September mainly at the thermocline depths between 100 and 150 m. The observed amplitude minimum could be related to a separation of the first barcolinic mode from other modes, as suggested by the linear theory of Gill (1984) stating that such a mode separation leads to a relative amplitude minimum.

Vertical phase distributions of the CW currents at the slope locations were rather complex over a time period between 14 and 27 September 2004, as Fig. 9 displays for M14 and M6. Before the hurricane reached the slope, the phases at different depths began to converge (Fig. 9a). Upon storm arrival, the phase difference between the mixed and thermocline layers was established, and, for example, the phase difference between 52 and 112 m was about 90° at M14 until 21 September, when the near-inertial motion began to weaken in the mixed layer. Furthermore, between 15 and 21 September the phase also decreased with increasing depth. The

rapid phase changes were between the bottom of the mixed layer and the upper thermocline. These rapid changes were observed between 82 and 132 m for M14, while deeper in the water column the decreasing phase trend with depth was much more gradual. Additionally, the phase below 350 m became less variable and showed a decrease with depth at M14 once the near-inertial motion strengthened on 17 September. On the same day and for the next two days, the phases in the thermocline and below were nearly in-phase and approximately 180° out of phase with those at 52 m. This phase distribution and amplitude structure at M14 indicated that the initial vertical response may have been in the form of a first baroclinic mode. As time progressed the response became more complex as higher baroclinic modes also became important, which was well reflected in the more complex vertical distributions of the amplitudes and phases at M14 on 20 September. Generally, the vertical structure of the phase at the other slope moorings had similar features as described for M14; however, the time of significant phase changes varied from one mooring to another.

The vertical distribution of the CW amplitudes and phases at all slope moorings was consistent with upward phase propagation and downward energy propagation from the mixed layer to the thermocline and below. These features have been commonly observed for near-inertial motions generated by other storms (see, e.g., Price 1983; Brooks 1983; Shay and Elsberry 1987). Energy flux from the mixed layer was estimated from a relationship given by $0.5\rho u^2 h T^{-1}$ (Shay and Elsberry 1987) where ρ is the density (1026 kg m^{-3}), u is amplitude of the near-inertial current in the mixed layer, h is the thickness of the mixed layer, and T is the e-folding time scale of energy. This flux was also asymmetric around the storm path and was roughly 0.012 W m^{-1} at M11 (T is equal to three inertial periods, u is 35 cm s^{-1}, h is 50 m) and 0.030 W m^{-1} at M14 (T is equal to four inertial periods, u is 50 cm s^{-1}, h is 80 m). The magnitude of the flux generated by Hurricane Ivan was comparable to the flux estimated for other hurricanes. For instance, Brooks (1983) estimated a flux of 0.01 W m^{-1} for Hurricane Allen, while Shay and Elsberry (1987) estimated a flux of 0.023 W m^{-1} for Hurricane Frederic.

The initial vertical phase difference between the mixed and thermocline layers (about 90°) implied that a vertical wavelength of the near-inertial waves on the slope generated by Hurricane Ivan exceeded 1 km. An initial phase difference between the currents near 50 m at M13 and M14 suggested that a horizontal wavelength might have been about 180 km. These wavelengths allowed us to estimate vertical and horizontal group velocities as defined by Brooks (1983), which, for a con-
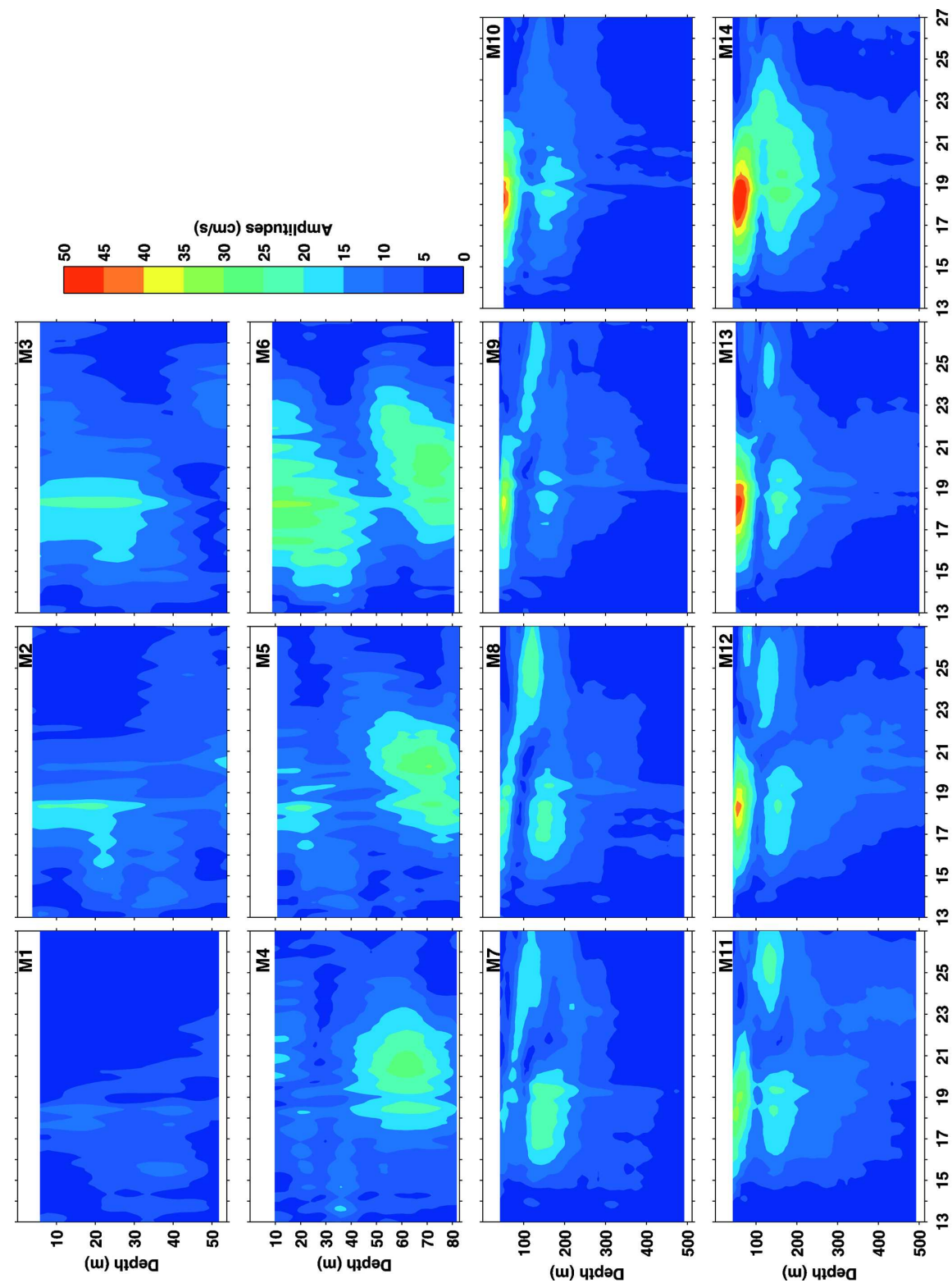
FIG. 8. Amplitude of the clockwise near-inertial motion (cm s^{-1}).
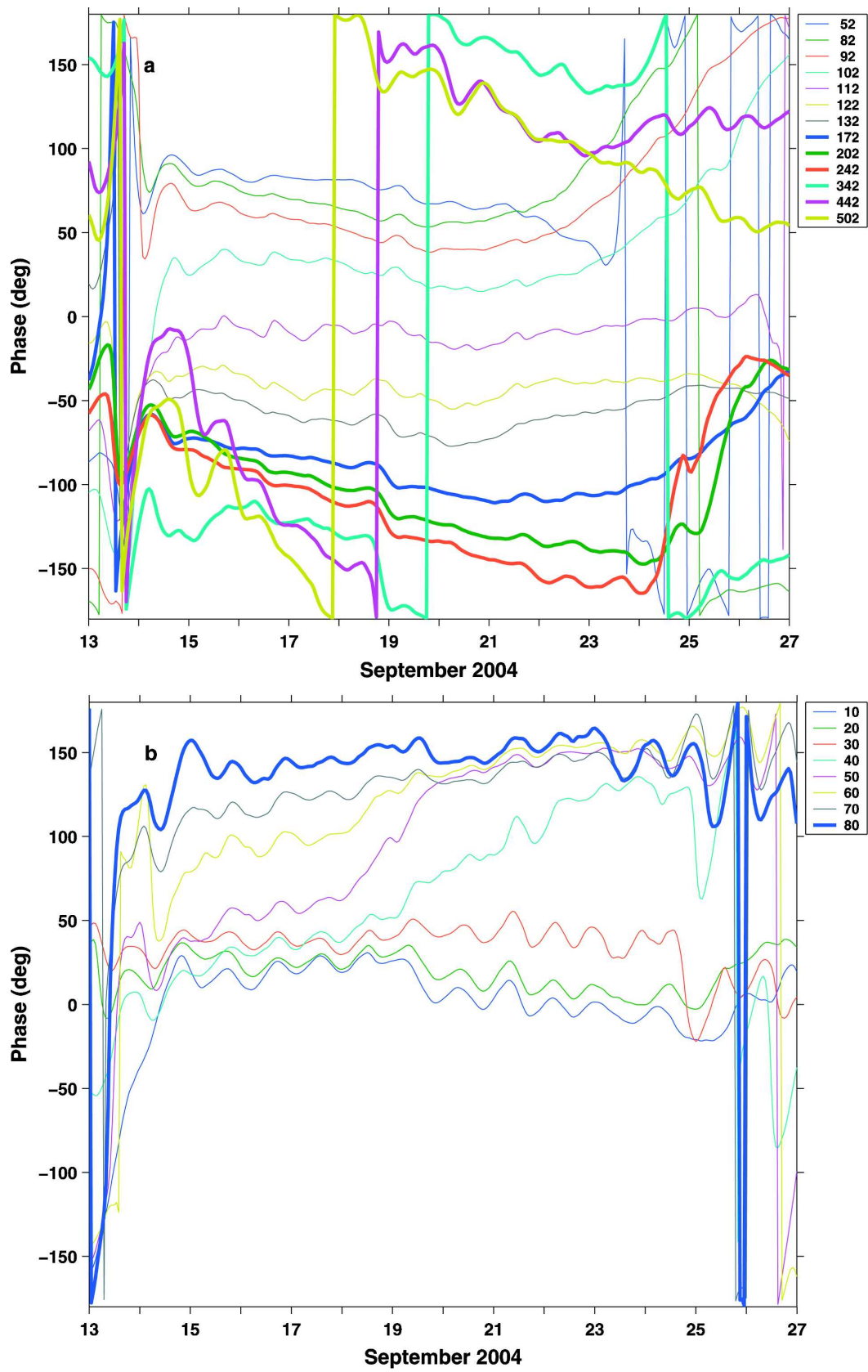
FIG. 9. Phase of the near-inertial motion for (a) mooring M14 and (b) mooring M6.

stant buoyancy frequency of 3.5 cph, were equal to -0.25 cm s^{-1} (a negative sign means downward energy propagation) and 0.45 m s^{-1}, respectively, while the vertical and horizontal phase velocities were about 1.2 cm s^{-1} and 2.1 m s^{-1}. These velocities are again comparable to those, for instance, evaluated for Hurricanes Allen (Brooks 1983) and Frederic (Shay and Elsberry 1987).

On the outer shelf, the maximum CW amplitudes (Fig. 8) peaked at 30 cm s^{-1} along L2 and at about 20 cm s^{-1} at L1. Along L1 the most energetic near-inertial motion was confined to the upper 40 m, while along L2 at M4 and M5 the motion was more intense below 40 m, especially after 17 September 2004. At M6 the inertial motion was initially surfaced intensified and then became bottom intensified. The different vertical structures among the shelf moorings were probably partly related to the wind stress rotation and partly to stratification. The influence of the wind stress rotation can be seen at M1 and M4 where the wind stress rotated counterclockwise during the forced stage of Hurricane Ivan, in the opposite direction of the currents resulting in weak near-inertial oscillations in the upper 40 m (Fig. 8). The energetic near-inertial fluctuations below 40 m, which were observed along L2 but not present along L1 between 17 and 23 September, were probably offshore propagating internal near-inertial waves that were generated somewhere between L1 and L2, such as at a location where a bottom front may have been formed. Davies and Xing (2005) have modeled such a scenario and have demonstrated that, with a coastal boundary and a bottom front present, wind-induced near-inertial oscillations and offshore propagating near-inertial waves can be easily be generated near such a front. They also showed that near-inertial currents below the thermocline are phase shifted by 180° from those above (nearly a 180° shift was observed at L2, and will be discussed in the next paragraph). Full water column temperature and salinity profiles were not available to resolve changes in stratification during the wake of Hurricane Ivan. However, SEED near-bottom temperature time series and satellite sea surface temperature suggested that the water column was either well mixed or very weakly stratified along L1, while along L2 the stratification was never fully destroyed by the hurricane winds. Thus a bottom front may have been present between these two lines and offshore propagating near-inertial waves could have been generated there and may have been responsible for the enhanced CW amplitudes below 40 m at M4, M5, and M6. Furthermore, the near-inertial oscillations decayed faster on the shelf than on the slope, especially those at the moorings deployed at 60-m water depth. This faster decay was partly related to proximity of the coastal boundary and partly to frictional effects.

Along L1, the near-inertial motions were nearly in-phase at depths where their amplitudes were above the background noise (>5 cm s^{-1}). Phase structures at the moorings deployed along L2 were more complex, such as shown for M6 in Fig. 9b. At this location the vertical phase structure indicated that the currents near the surface and bottom flowed nearly in the opposite directions between 15 and 25 September 2004 as the phase difference between the surface and bottom currents was between 130° and 160°. This phase difference along with the vertical distribution of the amplitudes suggested that the dominant vertical response at the near-inertial frequency may have been in the form of the first baroclinic mode at M6. Vertical phase distributions (not shown) at M4 and M5 displayed more variability than at M6. When energetic oscillations were present below 40 m at M4 and M5, phase differences between the near-surface and near-bottom currents were at least 120°. These differences indicate that the lowest baroclinic mode may also have contributed greatly to the vertical structure of the near-inertial motion at M4 and M5.

b. Subinertial waves

Another distinct feature observed along the slope during the relaxation stage was a subinertial wave (Figs. 5 and 6). This wave was probably partly a forced stage and partly a relaxation stage response of the ocean to Hurricane Ivan because evidence of its existence was found as early as in Stage 1 in the slope moorings where strong deep current maximums were present. A response in the form of subinertial waves to the passage of Hurricane Fran over the Gulf Stream was also described and modeled by Xie et al. (1999).

Wavelet analysis of the SEED temperature and current measurements showed that there was an energy peak present at periods between 2 and 5 days during and after Hurricane Ivan. The 2–5-day band passed velocities show the manifestation of the wave (Fig. 10). Similar energy peaks at about the same frequency were also present in SEED current records when Hurricanes Frances and Jeanne were affecting the eastern Gulf of Mexico. The 2–5-day band passed along-shelf velocity recorded by the 900-m Aanderaas instruments clearly showed the subinertial waves generated by these three hurricanes (Fig. 11).

The current data implied (Fig. 10) that the subinertial waves generated by Hurricane Ivan reached the SEED moorings around 0000 UTC 15 September 2004 and were present there for approximately 7 more days.
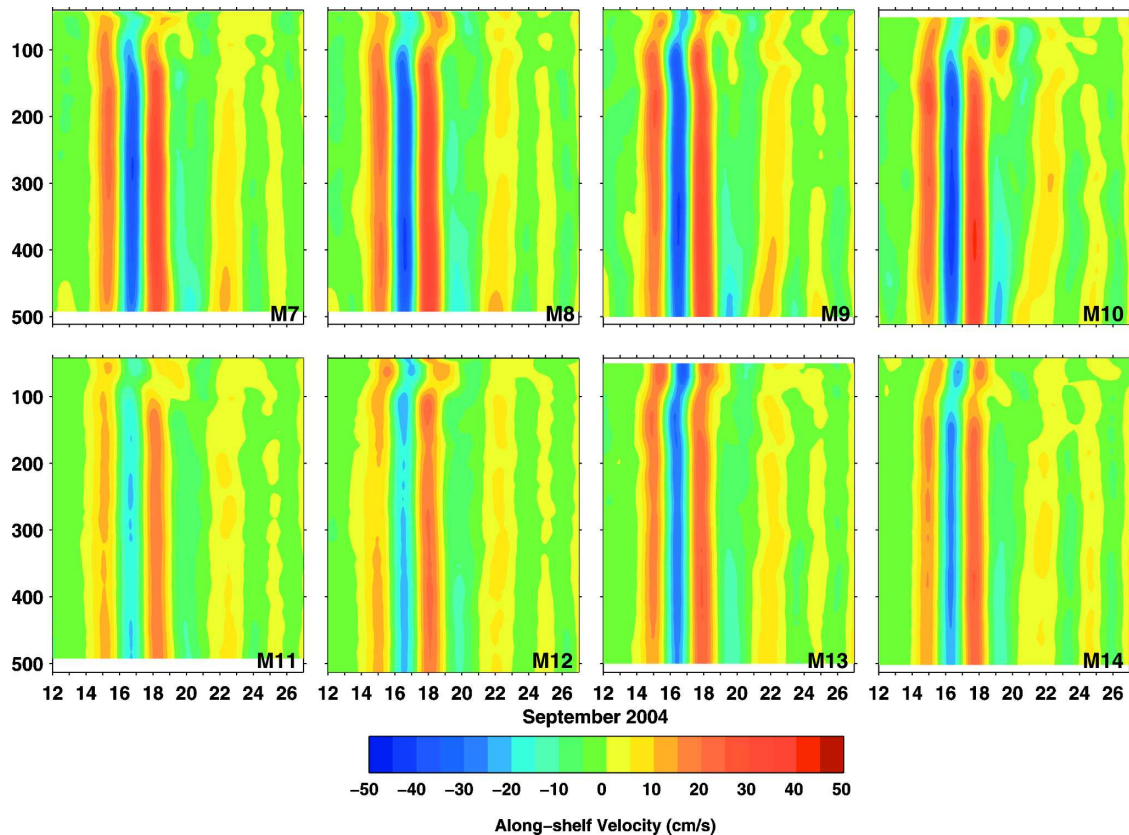
FIG. 10. The bandpassed (2–5 days) along-shelf velocity contours showing the subinertial waves with characteristics of TRWs generated by Hurricane Ivan.

These data also indicated that the horizontal kinetic energy of the subinertial waves was mainly contained in the along-shelf current component, which reached speeds of nearly 45 cm s^{-1} while the cross-shelf velocities did not exceed 10 cm s^{-1}. The largest speeds during Hurricane Ivan in the 2–5-day band were observed on the right side of the storm path generally below 100–150 m. The maximum velocities at the moorings with nearly full water column coverage (those deployed along the 500-m isobath) were found near 400 m below the sea surface. Additionally, complex correlation coefficient analysis of the current observations (the 2–5-day band passed data) between 29 August and 5 October along the 500-m and 1000-m isobaths indicated that the currents generally below 100–150 m were highly correlated (correlation coefficients 0.8 or higher), while the currents above these depths showed weaker or little correlation with those observed in the lower part of the water column. Veering angle differences between near-bottom currents and those below 100–150 m were rather small (generally less than 10°) and tended to increase rapidly with currents above about 100 m.

A single cross-spectral matrix with spectral estimates centered at 0.3871 cpd was generated for the slope currents (M7–M14) and then subjected to empirical orthogonal function (EOF) analysis (Denbo and Allen 1984; Hamilton 1984). Results indicated that about 88% of the current variance can be explained by the first EOF mode. Phases associated with this mode also suggested that the currents were practically in phase below 100–150 m (maximum phase differences less than 15°). Furthermore, they also implied that there was westward or downshelf and southward or offshelf phase propagation. Phase differences of the first EOF mode among the near-bottom currents were further utilized to estimate along-shelf and cross-shelf wavenumbers. Following Thompson (1977) and Hamilton (1984), a least squares method was used to find the best fit for these wavenumbers. These computations led to an along-shelf wavenumber of about −0.006 km^{-1} and a cross-shelf wavenumber of about −0.035 km^{-1}. The estimated wavenumbers were consistent with visual observations of the phase propagation and indicated that the evaluated wave vector pointed toward the southwest quadrant. The resulting horizontal wavelength was estimated to be about 28 km.
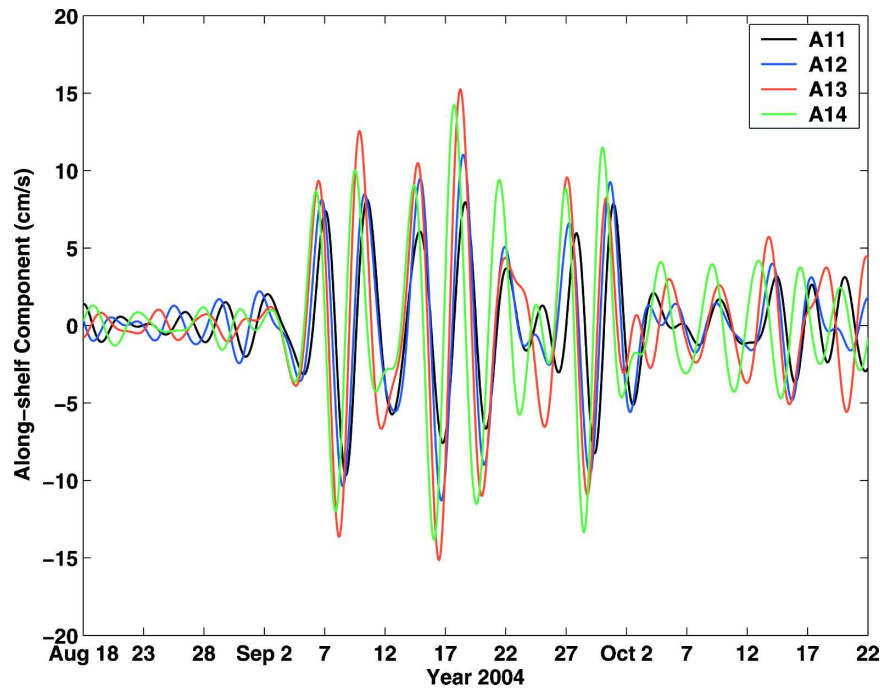
FIG. 11. The bandpassed (2–5 days) along-shelf velocity recorded by the 900-m Aanderaas instruments showing the subinertial waves generated by three hurricanes (Francis, Ivan, and Jeanne occurring on 6, 16, and 27 Sep, respectively).

These analyses have suggested that hurricanes observed in the Gulf of Mexico between 29 August and 5 October 2004 generated subinertial response in the form of topographic Rossby waves (TRWs; Rhines 1970). TRWs are important in ocean dynamics along the continental slope and rise when the bottom slope is sufficiently large to dominate the β effect. The observed waves had several characteristic of the TRWs, including 1) they were bottom-intensified (maximum speeds near 400 m along L3), 2) currents below 100–150 m were highly correlated and nearly in phase—thus the motion could be considered as columnar, which is characteristic of TRWs—and 3) the phase propagation was down- and offshelf.

Existence of TRWs in the gulf has been well documented (Hamilton 1990; Hamilton and Lugo-Fernandez 2001) and modeled (Oey and Lee 2002). Those TRWs, however, had much larger periods (>10 days), longer horizontal wavelengths (>100 km), and were observed farther offshore on the lower continental slope and rise. In addition, they were presumed to be generated by pulsations of the Loop Current (LC), the LC eddy shedding, and/or the LC eddies themselves (Hamilton 1990; Hamilton and Lugo-Fernandez 2001; Oey and Lee 2002). Estimation of the bottom slope (0.02 or larger) near the SEED moorings deployed along L3 and L4 indicated that the upper continental

slope can support TRWs with periods of 0.6 days and longer as evaluated from $\omega = \alpha N$ where ω is the maximum frequency, α is the bottom slope, and N is the buoyancy frequency taken as 10^{-3} s^{-1}. Here N was estimated from hydrographic data collected during SEED cruises and historical salinity and temperature data (Jochens et al. 2002). The TRW dispersion relation (Rhines 1970),

$$\omega = k\alpha N K_H^{-1} \coth(f^{-1}NHK_H), \qquad (2)$$

where k is the along-shelf wavenumber and K_H is the horizontal wavenumber (both estimated earlier), H is the water depth taken to be 1000 m, α is the bottom slope of 0.02, and f is the Coriolis parameter of 1.13×10^{-5} s^{-1}, yielded a wave period of 3.4 days. This period is in agreement with results from the wavelet analysis that showed the energy peaks occurred for periods between 2 and 5 days. Additionally, estimates of the along-shelf and cross-shelf components of group velocities were -0.55 and 0.12 m s^{-1}, which indicated that the wave energy propagated basically downshelf and slightly upslope (onshelf) near the SEED moorings. These wave characteristics implied that the subinertial waves were probably generated by the storms somewhere in the eastern part of the Gulf of Mexico.
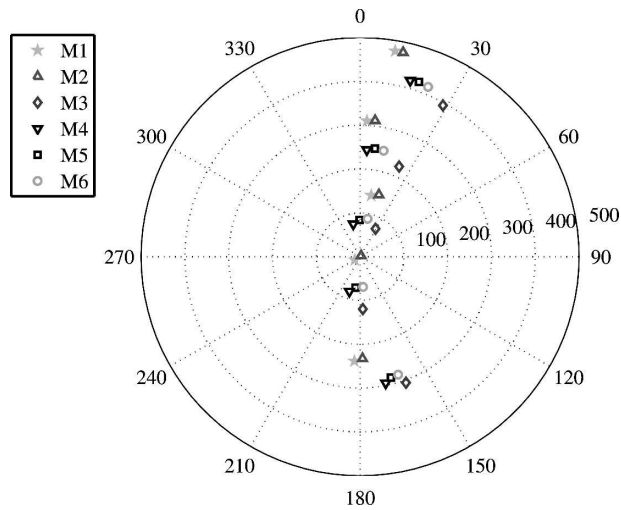
FIG. 12. Polar plot of the relative locations of wave measurements from the SEED moorings with respect to Ivan's center and its forward direction.

7. Bottom scour

Bottom scour results from a combination of wave-driven sediment resuspension and current-driven transport of the resuspended sediment (Keen and Glenn 2002). Waves generated by Ivan were the largest ever measured and were more than adequate to resuspend sediment over all six moorings (Wang et al. 2005).

Near-bottom currents forced by Ivan ranged from 40 to 120 cm s^{-1} at the moorings (Teague et al. 2006a) and were sufficient to transport the resuspended sediment and generate scour. The combination of pressure, wave, and near-bottom current data from our measurements allowed for bottom scour to be evaluated. Pressure measurements showed that the depth of the six shelf moorings increased after the passage of Ivan. The moorings with the greatest depth change did not release normally from the bottom due to sediment (mostly sand) filling open spaces inside the Barny and affecting the release mechanisms. These two moorings were recovered using a remotely operated vehicle (ROV), which also provided video monitoring of the recovery and revealed that the moorings were resting normally on the bottom, were not buried in sediment, and showed no localized scour (the moorings were not sitting in small depressions). In addition, internal attitude (pitch/roll) sensors contained in the ADCPs fluctuated by several degrees during the passage of Ivan but remained steady prior to and after the passage of Ivan. Hence, the scour determined from our measurements was credible.

Bottom scour at the moorings is discussed in detail by Teague et al. (2006b). In summary, significant bottom scours of 8, 32, 36 cm were found at water depths of about 60 m at moorings M1, M2, and M3, respectively, and 8, 8, and 9 cm at depths of about 90 m at moorings
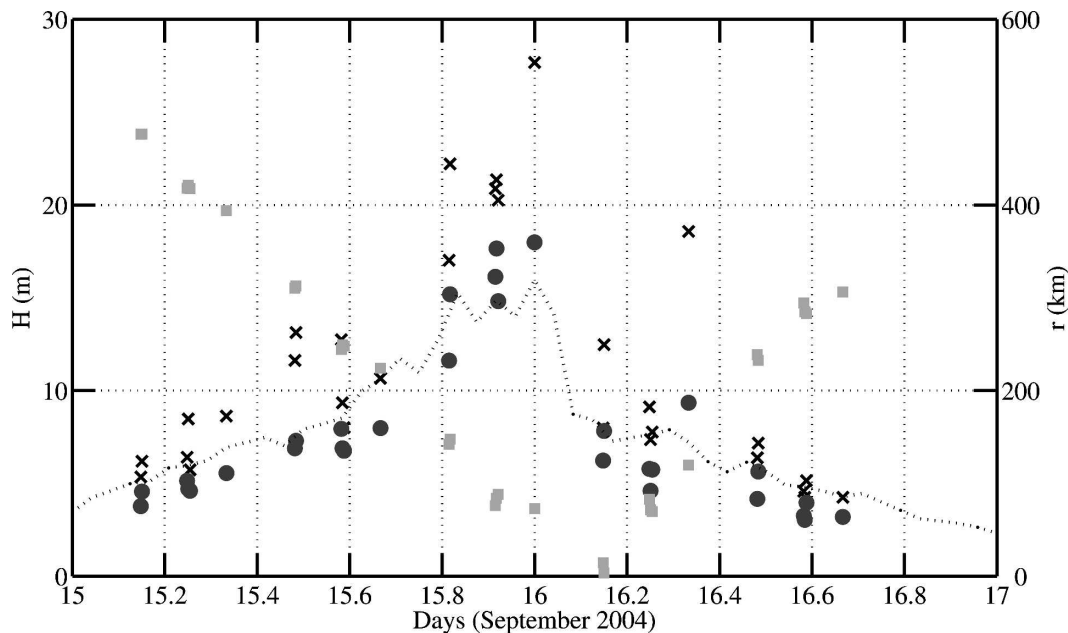

FIG. 13. Time evolution of extreme seas at the SEED moorings during the passage of Ivan. Solid circles: significant wave heights (H_s); crosses: maximum wave height (H_{max}); dotted line: significant wave height from NDBC 42040; solid squares: the distance to Ivan's center (r).

TABLE 3. Hurricane Ivan parameters and relative locations of moorings at times of extreme wave measurements. Time: starting time of data acquisition (15 Sep 2004), R: mooring distance to Ivan's eye at the data acquisition time, Θ: azimuth angle from the eye to the mooring with respect to north, P_c: Ivan's center air pressure, V_f: Ivan's forward moving speed, and θ_f: Ivan's forward moving direction with respect to the north.

Mooring	Time (UTC)	R (km)	Θ (°)	P_c (hPa)	V_f (m s^{-1})	θ_f (°)
M3	2359:55	73	29	931	3.08	0
M4	2157:51	76	0	932	6.30	12
M5	2201:14	84	11	932	6.30	12
M6	2206:45	88	23	932	6.12	12

M4, M5, and M6, respectively. The maximum wind stress occurred to the right of the eye, at moorings M2, M3, and M6, where the scour was greatest. Sediment was generally transported southwestward, toward the Mississippi River Delta, suggesting a depositing of sediment near the shelf break.

Scour has been generally thought to be insignificant at depths below 60 m, and it has been reflected by engineering studies that do not require pipelines to be buried at these depths. However, significant bottom scour of sandy surfaces during hurricanes will occur when orbital wave velocities generate sediment resuspension and the background mean flow conditions are

sufficient to transport the suspended sediment regardless of the actual depth of the bottom. Since orbital velocity decays exponentially with depth, only extremely intense hurricanes like Ivan should generate the conditions that lead to scour at depths of 60 and 90 m as observed here.

8. Surface gravity wave observations

The passage of an intense hurricane's eye over securely moored instruments also provided the rare opportunity for in situ measurements of extreme surface waves generated near the center of the storm. Hurricane-generated surface waves were measured by the wave/tide gauges mounted in the six shelf moorings (M1, M2, M3, M4, M5, and M6). Ivan approached the moorings with a nearly steady intensity and forward speed. The relative location of the moorings with respect to the Ivan's center and its forward direction at times of data acquisition are shown in polar coordinates in Fig. 12. The wave data were mainly recorded within a narrow window located in Ivan's front-right quadrant
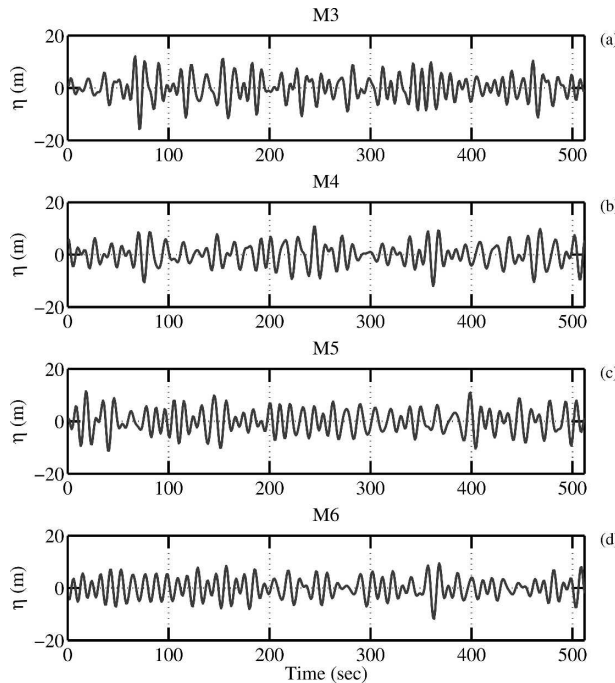

FIG. 14. Time series of surface waves from extreme seas at the SEED mooring M3, M4, M5, and M6.

TABLE 4. Statistical parameters from the extreme seas at the SEED moorings derived from the 512-s time series of surface wave elevations; N: number of individual waves based on the zero-upcrossing definition, N_{15}: number of individual waves with heights larger than 15 m, H_{max}, T_{max}: the maximum wave height and its associated wave period, $H_{1/10}$, $T_{1/10}$: average values of the highest one-tenth of the wave heights and associated wave period, $H_{1/3}$, $T_{1/3}$: average value of the highest one-third of the wave heights and associated wave period, H_{avg}, T_{avg}: average wave heights and average wave periods, H_s: significant wave height calculated as 4 times the rms of η, T_p: peak period of wave spectra, T_{m1}: mean wave period based on the first moment of the wave spectrum, and T_{m2}: mean wave period based on the second moment of wave spectrum. (All heights are in meters and periods are in seconds.)

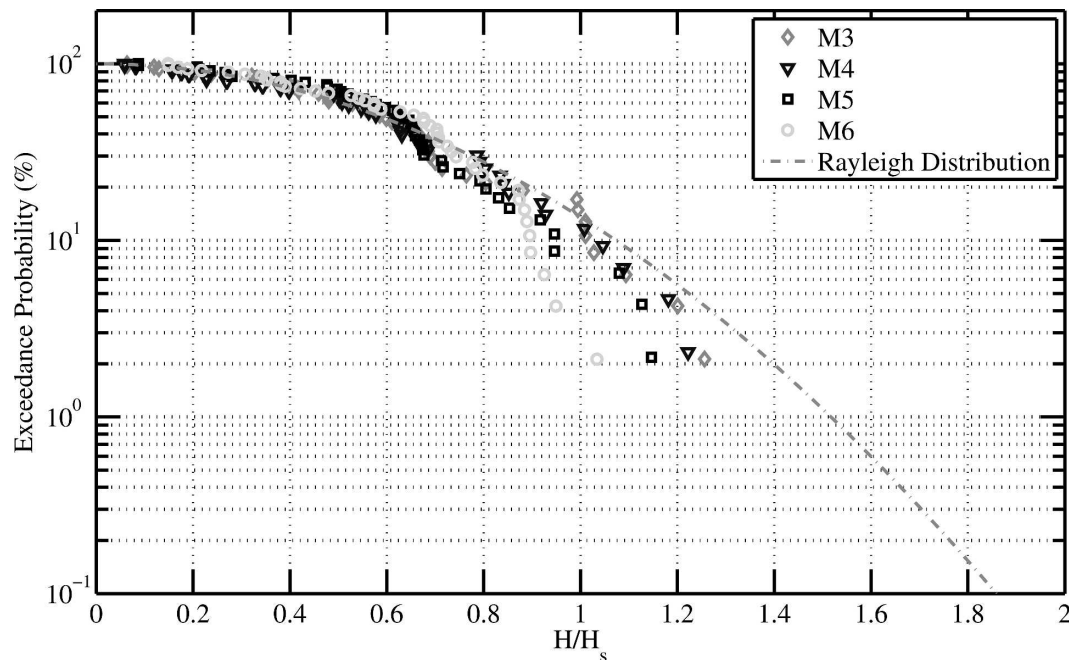| Parameters	M3	M4	M5	M6
N	47	43	46	47
N_{15}	10	6	8	2
H_{max}	27.7	20.9	21.4	20.3
$H_{1/10}$	22.0	19.3	19.5	15.3
$H_{1/3}$	17.2	15.7	15.9	13.2
H_{avg}	11.2	9.7	11.0	9.2
H_s	18.0	16.1	17.7	14.8
T_{max}	10.1	11.0	11.9	12.1
$T_{1/10}$	10.5	11.5	12.1	10.8
$T_{1/3}$	11.3	12.4	11.2	10.8
T_{avg}	10.4	11.7	11.0	11.7
T_{m1}	10.7	11.9	11.7	11.3
T_{m2}	10.3	11.6	11.5	11.1
T_p	14.8	13.6	14.8	9.2
Spectral width ν	0.26	0.23	0.21	0.19
Skewness λ_3	−0.15	−0.08	0.00	−0.02
Kurtosis λ_4	3.18	2.86	2.47	2.56

FIG. 15. Exceedance probability of individual wave height (normalized by H_s) from the extreme seas at the SEED moorings. The Rayleigh probability distribution is shown as the dashed–dotted line.

during its approach. The temporal evolution of extreme seas over the moorings is depicted by a time history of significant wave height (H_s) and maximum individual wave height (H_{max}) (Fig. 13). Significant wave height is calculated as four times the root mean square of η. The individual crest-to-trough wave height (H) is defined as the elevation range between two zero upcrossings. As Ivan approached the moorings, H_s increased from about 5 m to about 18 m and then dropped significantly as the eye moved over the moorings. The maximum measured H_s from moorings M3, M4, M5, and M6 reached 18.0, 16.1, 17.7, and 14.8 m, respectively, just prior to the arrival of Ivan. A wave height of 27.74 m, the largest wave height ever directly measured with instrumentation, was recorded at M3 (Wang et al. 2005). Hourly wave measurements from National Data Buoy Center (NDBC) buoy 42040 are also shown. The buoy recorded H_s of 15.96 m, the largest ever reported by an NDBC buoy prior to Hurricane Katrina in 2005.

Four 512-s wave measurements from moorings M3, M4, M5, and M6 located near the forward face of Ivan and near the eyewall (Fig. 12; Table 3) were selected for detailed analyses here. The time series of η for the 512-s records (sampled at 1 Hz) for moorings M3, M4, M5, and M6 are shown in Fig. 14. The number of individual waves for the four datasets ranged from 43 to 47 (Table 4). The number of individual waves larger than 15 m ranged from 10 at M3 to 2 at M6. Out of total 183 individual waves from these four datasets, there were

26 individual waves with heights larger than 15 m. The distribution of η generally followed a normal distribution with skewness (λ_3) near 0 and kurtosis (λ_4) closer to 3 (Ochi 1998). Smaller values of λ_4 were found at M5 and M6 (Table 4). The distribution of H was compared against the Rayleigh distribution (Ochi 1998) in Fig. 15. For smaller H, the agreement between hurricane wave data and the Rayleigh distribution was very good. As wave heights increased (larger than $0.8H_s$), the probability distribution of H was smaller than that predicted by the Rayleigh distribution. The underestimation increased at larger wave heights and was more pronounced for M6. However, wave breaking was expected to be very active under strong wind conditions, which could limit the numbers and magnitudes of large waves. In addition, waves could have been underestimated since higher frequency wave components could not be measured by the bottom-mounted wave gauges (high-frequency cutoff are 0.12 and 0.14 Hz, respectively, for moorings at 60-m and 90-m depth). Nevertheless, this comparison showed that the probability and magnitude of extremely large waves reported here were well within the prediction of the Rayleigh distribution. Therefore, this implied that these large waves were not rogue waves.

The joint distribution of the individual wave heights H and their associated wave periods T provided further details of extreme seas that are of great importance to the safety design of floating marine structures (Ochi
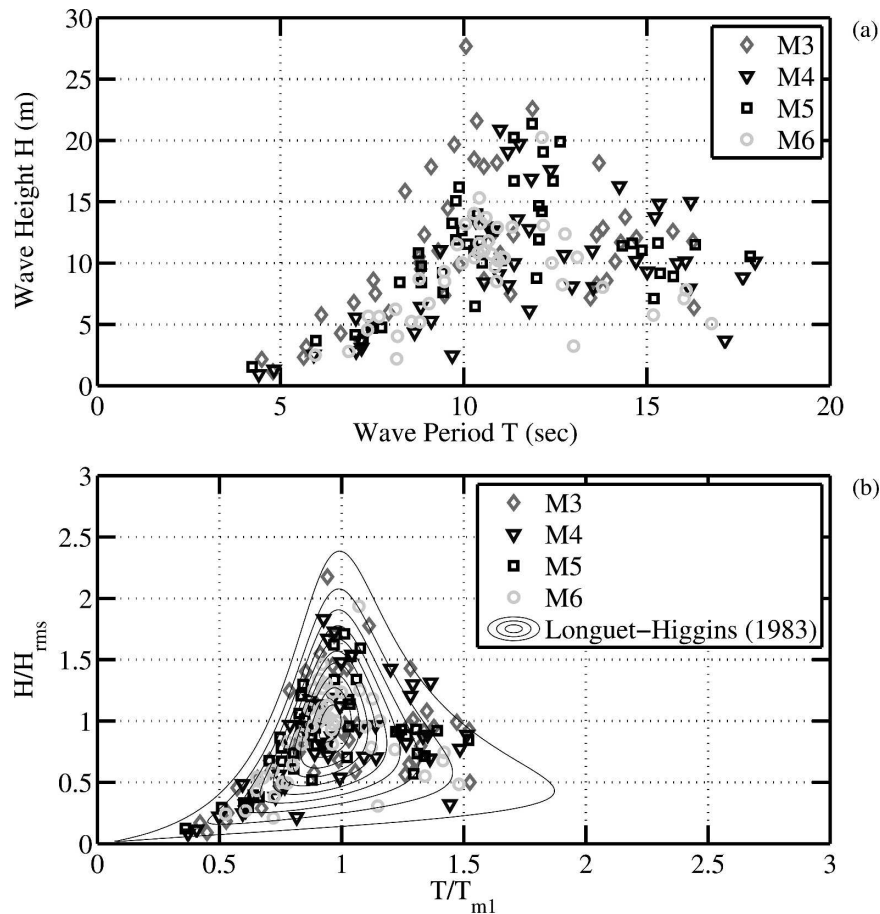
FIG. 16. (a) Scatterplot of individual wave heights vs their associated wave period, and (b) scatterplot of normalized wave height vs normalized wave period; H_{rms} is the root-mean-square wave height and is estimated by $H_s/\sqrt{2}$ and T_{m1} is the mean wave period, respectively (see Table 4). The contours represent the dimensionless joint probability function of wave height and period (Longuet-Higgins 1983). Outermost contour is for a joint probability density of 0.1. Subsequent contours are at 0.2 intervals.

1998). Wave height versus wave period for the four selected moorings is shown in Fig. 16a. The periods associated with extreme waves (>20 m) ranged from 10 to 12 s. The joint probability function proposed by Longuet-Higgins (1983) was plotted against the normalized wave height and wave period in Fig. 16b. Our data were well within the boundary encompassed by the joint probability function.

The analysis of the four time series of η from extreme seas and the comparisons against the commonly used normal and Rayleigh distributions, and the joint probability function (Longuet-Higgins 1983) suggested that these extreme large waves were from a typical wave population closely following the normal and Rayleigh distributions. This implied that the extremely large waves measured during Ivan were not "freak" waves with extremely low probability of occurrence. Instead,

they occurred well within the limits of typical wave populations. The impression that our measurements could be "freak" is probably attributed more to the difficulties in collecting such data than to the rarity of such waves. The wave-sampling strategy used here sampled every 8 h and thus sampled only a relatively small population of the hurricane wave field. This suggested that our measurements likely missed the largest waves near the storm's eyewall, and that even larger surface waves could be commonly generated by intensive hurricanes. Nevertheless, these storm data and the associated statistics should prove valuable for further studies.

The wave data were also used to approximately depict spatial variation of a hurricane wave field at distances ranging from 500 km to its core center. A radial profile of Ivan's wave field, approximately represented
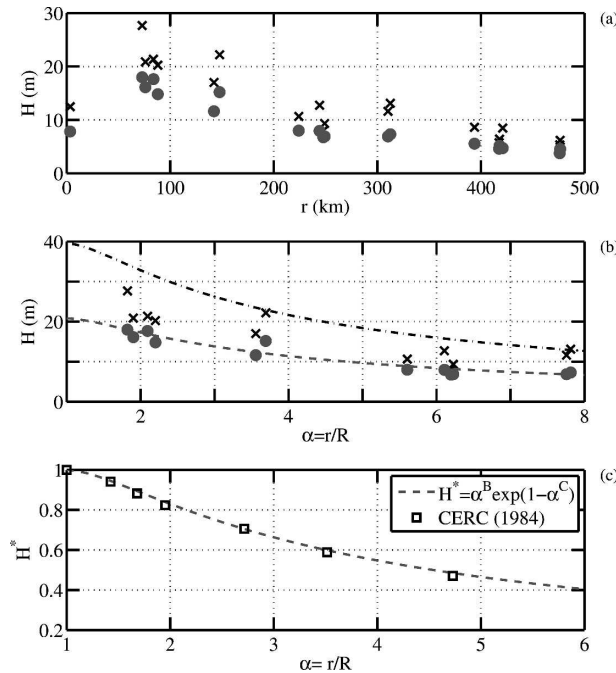
FIG. 17. The radial profile of hurricane wave field: (a) wave heights (H) vs radial distance (r); (b) wave height (H) vs normalized radial distance ($\alpha = r/R$). The dashed line represents the exponential relation [(3)]. The dashed–dotted line represents $H_{max} = 1.9H_s$. (c) Normalized wave height (H^*) vs normalized radial distance. Solid circles: significant wave height (H_s); crosses: maximum wave height (H_{max}); squares: wave model (CERC).

as wave heights H_s and H_{max} versus the radial distance, r, to the hurricane eye, is shown in Fig. 17a. Here H_s and H_{max} increased rapidly as r decreased from about 500 km and peaked at about 70 km. Both H_s and H_{max} became smaller at Ivan's center as r approached zero. The wave radial profile can be further expressed as a function of a nondimensional distance given by $\alpha = r/R$ (Fig. 17b); R is the radius of hurricane eye estimated as the radial distance from the center of the eye to the eyewall, where the wind speed is the strongest. For Ivan, R was about 40 km. Owing to the small amount of wave data near the center of Ivan, attention is focused on the wave radial profile outside of the eyewall where $\alpha \geq 1$. An exponential function that approximates the radial profile as a function of α was formulated and is

$$H_s = A\alpha^B \exp(-\alpha^C) \quad \text{for} \quad \alpha \geq 1, \qquad (3)$$

where the empirical coefficients are $A = 56.61$ m, $B = -0.96$, and $C = -0.94$. Equation (3) is represented by the dashed line in Fig. 17b. Based on past observations of hurricanes, an upper limit of maximum wave height H_{max} was proposed as $1.9H_s$ (dashed–dotted line; Bea 1974). This upper limit compares well with our measured H_{max}. The wave radial profile in (3) can be fur-

ther normalized by the H_s at the radius of the hurricane eyewall ($\alpha = 1$), and is

$$(H_s)_{max} = A \exp(-1). \qquad (4)$$

The normalized hurricane wave field radial profile can then be expressed as

$$H^* = \alpha^B \exp(1 - \alpha^C), \qquad (5)$$

where H^* is the normalized $H_s/(H_s)_{max}$. This result (Fig. 17c) compared well with a wave radial profile along the line with an angle of 15° to the right of the hurricane's forward direction extracted from a simulated wave field [Coastal Engineering Research Center 1984]. The radial dependence and the coefficients in (3) and (5) are likely different on the left-hand side of the hurricane.

9. Summary and conclusions

Hurricane Ivan forced currents in excess of 200 cm s^{-1} on the shelf and currents almost as large on the slope. Currents on the outer shelf were frictionally dominated, followed Ekman dynamics, and were not geostrophically balanced during the passage of Ivan. During the approach of Ivan, flow on the outer shelf consisted of overlapping Ekman surface and bottom boundary layers. As the eye of Ivan passed over the moorings, the surface Ekman layer extended almost to the bottom on the shelf and deepened on the slope to about 90 m. Below the surface Ekman layer on the slope, a strong downshelf flow with speeds in the vicinity of 100 cm s^{-1} was established. Near-inertial oscillations lasting about 10 days with amplitudes of about 50 cm s^{-1} were generated at the onset of Ivan on the shelf and slope but were not prominent until after Ivan had passed. Subinertial waves having several characteristic of TRWs, with periods of 2–5 days and horizontal wavelengths of about 28 km, were triggered by Ivan as it approached the array and resulted in strongest downshelf flow with speeds of about 45 cm s^{-1} along the slope about a day after Ivan passed over the moorings. These subinertial waves can be expected to play an important role in the dynamics along the upper slope, perhaps affecting the entire northern Gulf of Mexico shelf during hurricane passage. Currents observed during the forced stage response were stronger to the left of the track on the shelf due to topographic constraints and more energetic to the right of the track, as expected, on the slope. Surface waves during Ivan were the largest ever directly measured, and the wave analyses revealed that the record wave height of 27.7 m was not a rogue wave but rather a common wave under intense storms. The combination of large orbital wave velocities associated with big waves and large hurri-

cane-generated near-bottom currents caused significant bottom scour of 36 cm at 60-m water depth.

The extreme currents, waves, and scour associated with Hurricane Ivan can also be expected with other similar size storms and, perhaps most important, can be exceeded if the more intense category-5 hurricanes in the Gulf of Mexico can maintain their intensity when they are near the coast. Our analyses indicate that the criteria for 100-yr return frequency need to be redefined given the increasing number of offshore structures in the gulf and our dependence on the energy production in the Gulf of Mexico. Current and wave statistics of extreme seas under the center of intense hurricanes are invaluable for expanding our knowledge of ocean dynamics, evaluating and developing storm models, and for setting standards that will improve the design and safety of offshore operations.

REFERENCES

Bea, R. G., 1974: Gulf of Mexico hurricane wave heights. *Proc. Sixth Offshore Technology Conf.,* Houston, TX, Offshore Technology Conference (Paper OTC2110), 791–810.

Brink, K. H., 1989: Observations of the response of thermocline currents to a hurricane. *J. Phys. Oceanogr.,* **19,** 1017–1022.

Brooks, D. A., 1983: The wake of Hurricane Allen in the western Gulf of Mexico. *J. Phys. Oceanogr.,* **13,** 117–129.

Coastal Engineering Research Center, 1984: *Shore Protection Manual.* Vol. 1. U.S. Army Corps of Engineers, U.S. Government Printing Office, 608 pp.

Church, J. A., T. M. Joyce, and J. F. Price, 1989: Current and density observations across the wake of Hurricane Gay. *J. Phys. Oceanogr.,* **19,** 259–265.

Cooper, C., and J. D. Thompson, 1989: Hurricane-generated currents on the outer continental shelf. I. Model formulation and verification. *J. Geophys. Res.,* **94,** 12 513–12 539.

Davies, A. M., and J. Xing, 2005: The effect of a bottom shelf front upon the generation and propagation of near-inertial internal waves in the coastal ocean. *J. Phys. Oceanogr.,* **35,** 976–990.

Dean, R. G., and R. A. Dalrymple, 1991: *Water Wave Mechanics for Engineers and Scientists*. World Scientific, 353 pp.

Denbo, D. W., and J. S. Allen, 1984: Rotary empirical orthogonal function analysis of currents near the Oregon coast. *J. Phys. Oceanogr.,* **14,** 35–46.

DiMarco, S. F., E. Meza, and J. Zhang, 2001: Estimating wave elevation from pressure using second order nonlinear wave-interaction theory with applications to Hurricane Andrew. *J. Coastal Res.,* **17,** 658–671.

Donelan, M. A., B. K. Haus, N. Reul, W. J. Plant, M. Stiassnie, H. C. Graber, O. B. Brown, and E. S. Saltzman, 2004: On the limiting aerodynamic roughness of the ocean in very strong winds. *Geophys. Res. Lett.,* **31,** L18306, doi:10.1029/2004GL019460.

Emanuel, K. A., 1988: Toward a general theory of hurricanes. *Amer. Sci.,* **76,** 370–379.

Emery, W. J., and R. E. Thomson, 2001: *Data Analysis Methods in Physical Oceanography*. Elsevier, 640 pp.

Forristall, G. Z., 1980: A two-layer model for hurricane-driven currents on an irregular grid. *J. Phys. Oceanogr.,* **10,** 1417–1438.

——, R. D. Larrabee, and R. S. Mercier, 1991: Combined oceanographic criteria for deep water structures in the Gulf of Mexico. *The 23d Offshore Technology Conf.,* Houston, TX, Offshore Technology Conference (Paper OTC6541), 377–390.

Geisler, J. E., 1970: Linear theory of the response of a two-layer ocean to a moving hurricane. *Geophys. Fluid Dyn.,* **1,** 249–272.

Gill, A. E., 1984: On the behavior of internal waves in the wakes of storms. *J. Phys. Oceanogr.,* **14,** 1129–1151.

Greatbatch, R. J., 1984: On the response of the ocean to a moving storm: Parameters and scales. *J. Phys. Oceanogr.,* **14,** 59–78.

Hamilton, P., 1984: Topographic and inertial waves on the continental rise of the Mid-Atlantic Bight. *J. Geophys. Res.,* **89** (C1), 695–710.

——, 1990: Deep currents in the Gulf of Mexico. *J. Phys. Oceanogr.,* **20,** 1087–1104.

——, and A. Lugo-Fernandez, 2001: Observations of high speed deep currents in the northern Gulf of Mexico. *Geophys. Res. Lett.,* **28,** 2867–2870.

Jarosz, E., D. A. Mitchell, D. W. Wang, and W. J. Teague, 2007: Bottom-up determination of air-sea momentum exchange under a major tropical cyclone. *Science,* **315,** 1707–1709.

Jochens, A. E., S. F. DiMarco, W. D. Nowlin Jr., R. O. Reid, and M. C. Kennicutt II, 2002: Northeastern Gulf of Mexico chemical oceanography and hydrography study: Synthesis report. Minerals Management Service, Gulf of Mexico OCS Region Rep. 2002-055, 586 pp.

Keen, T. R., and S. M. Glenn, 1994: A coupled hydrodynamic–bottom boundary layer model of Ekman flow on stratified continental shelves. *J. Phys. Oceanogr.,* **24,** 1732–1749.

——, and ——, 1995: A coupled hydrodynamic–bottom boundary layer model of storm and tidal flow in the Middle Atlantic Bight of North America. *J. Phys. Oceanogr.,* **25,** 391–406.

——, and ——, 1999: Shallow water currents during Hurricane Andrew. *J. Geophys. Res.,* **104,** 23 443–23 458.

——, and S. E. Allen, 2000: The generation of internal waves on the continental shelf by Hurricane Andrew. *J. Geophys. Res.,* **105,** 26 203–26 224.

——, and S. M. Glenn, 2002: Predicting bed scour on the continental shelf during Hurricane Andrew. *J. Waterway, Port, Coastal, Ocean Eng. ASCE,* **128,** 249–257.

Kunze, E., 1985: Near-inertial wave propagation in geostrophic shear. *J. Phys. Oceanogr.,* **15,** 544–565.

Longuet-Higgins, M. S., 1983: On the joint distribution of wave periods and amplitudes in a random wave field. *Proc. Roy. Soc. London,* **389A,** 241–258.

Mitchell, D. A., W. J. Teague, E. Jarosz, and D. W. Wang, 2005: Observed currents over the outer continental shelf during

Hurricane Ivan. *Geophys. Res. Lett.,* **32,** L11610, doi:10.1029/2005GL023014.

Mooers, C. N. K., 1975: Several effects of a baroclinic current on the cross-stream propagation of inertial-internal waves. *Geophys. Fluid Dyn.,* **6,** 245–275.

Ochi, M. K., 1998: *Ocean Waves: The Stochastic Approach.* Ocean Technology Series, Vol. 6, Cambridge University Press, 319 pp.

Oey, L.-Y., and H.-C. Lee, 2002: Deep eddy energy and topographic Rossby waves in the Gulf of Mexico. *J. Phys. Oceanogr.,* **32,** 3499–3527.

Pawlowicz, R., B. Beardsly, and S. Lentz, 2002: Classical tidal harmonic analysis including error estimates in MATLAB using T_TIDE. *Comput. Geosci.,* **28,** 929–937.

Pedlosky, J., 1987: *Geophysical Fluid Dynamics.* 2d ed. Springer-Verlag, 710 pp.

Perkins, H., F. De Strobel, and L. Gauldesi, 2000: The barny sentinal trawl-resistant ADCP bottom mount: Design, testing, and application. *IEEE J. Oceanic Eng.,* **25,** 430–436.

Powell, M. D., S. H. Houston, L. R. Amat, and N. Morisseau-Leroy, 1998: The HRD real-time hurricane wind analysis system. *J. Wind Eng. Ind. Aerodyn.,* **77&78,** 53–64.

Price, J. F., 1983: Internal wave wake of a moving storm. Part I. Scales, energy budget and observations. *J. Phys. Oceanogr.,* **13,** 949–965.

——, T. B. Sanford, and G. Z. Forristall, 1994: Forced stage response to a moving hurricane. *J. Phys. Oceanogr.,* **24,** 233–260.

Rhines, P. B., 1970: Edge, bottom, and Rossby waves in a rotating stratified fluid. *Geophys. Fluid Dyn.,* **1,** 273–302.

Sanford, T. B., P. G. Black, J. R. Haustein, J. W. Feeney, G. Z. Forristall, and J. F. Price, 1987: Ocean response to a hurricane. Part I: Observations. *J. Phys. Oceanogr.,* **17,** 2065–2083.

Shay, L. K., and R. L. Elsberry, 1987: Near-inertial ocean current response to Hurricane Frederic. *J. Phys. Oceanogr.,* **17,** 1249–1269.

——, ——, and P. G. Black, 1989: Vertical structure of the ocean current response to a hurricane. *J. Phys. Oceanogr.,* **19,** 649–669.

Shen, C. Y., and T. E. Evans, 2001: Surface-to-subsurface velocity projection for shallow water currents. *J. Geophys. Res.,* **106,** 6973–6984.

Stone, G. W., and Coauthors, 2005: Hurricane Ivan's impact along the northern Gulf of Mexico. *Eos, Trans. Amer. Geophys. Union,* **86,** 497–508.

Teague, W. J., E. Jarosz, M. R. Carnes, D. A. Mitchell, and P. J. Hogan, 2006a: Low-frequency current variability observed at the shelfbreak in the northeastern Gulf of Mexico: May–October 2004. *Cont. Shelf Res.,* **26,** 2559–2582.

——, ——, T. R. Keen, D. W. Wang, and M. S. Hulbert, 2006b: Bottom scour observed under Hurricane Ivan. *Geophys. Res. Lett.,* **33,** L07607, doi:10.1029/2005GL025281.

Thompson, R. O. R. Y., 1977: Observations of Rossby waves near site D. *Prog. Oceanogr.,* **7,** 135–162.

Wang, D. W., D. A. Mitchell, W. J. Teague, E. Jarosz, and M. S. Hulbert, 2005: Extreme waves under Hurricane Ivan. *Science,* **309,** 896.

Xie, L., L. J. Pietrafesa, and C. Zhang, 1999: Subinertial response of the Gulf Stream system to Hurricane Fran of 1996. *Geophys. Res. Lett.,* **26,** 3457–3460.